

1  
2  
3  
4  
5  
6  
7  
8  
9  
10  
11  
12  
13  
14  
15  
16  
17  
18  
19

**Spectroscopic Analysis of Allophane and Imogolite Samples with Variable Fe Abundance  
for Characterizing the Poorly Crystalline Components on Mars**

Revision 1

Thomas Jeute<sup>1</sup>, Leslie L. Baker<sup>1</sup>, Janice L. Bishop<sup>2</sup>, Zaenal Abidin<sup>3</sup>, Elizabeth B. Rampe<sup>4</sup>

<sup>1</sup>Department of Geological Sciences, University of Idaho, 875 Perimeter Drive MS 3022,  
Moscow, Idaho, 83843

<sup>2</sup>SETI Institute, Mountain View, CA, USA, and National Aeronautics and Space  
Administration's Ames Research Center, Moffett Field, CA, USA

<sup>3</sup>Department of Chemistry, Faculty of Mathematics and Natural Sciences, Bogor Agricultural  
University, Indonesia

<sup>4</sup>National Aeronautics and Space Administration–Johnson Space Center, Houston, TX, USA

Submitted to American Mineralogist in revised form

May, 2020

Keywords: Mars, spectroscopy, nanophase, allophane, imogolite

20  
21  
22  
23  
24  
25  
26  
27  
28  
29  
30  
31  
32  
33  
34  
35  
36  
37  
38  
39  
40  
41

## Abstract

Nanophase materials including silicates, aluminosilicates, and iron oxides are widespread on Mars. These minerals are important because they likely represent a solid-phase record of ancient climatic conditions on the martian surface. Identification and characterization of nanophase compounds is technically challenging due to the small size and poorly ordered nature of these materials, particularly because their chemical compositions can vary widely.

This study presents spectra of several synthetic allophane and imogolite samples with a range of chemical compositions that are typical of the natural variability of allophanic materials. These samples were formed under controlled conditions and have been thoroughly characterized in terms of chemical composition and atomic structure.

Analyses confirmed that the synthetic materials were allophane and imogolite and were structurally similar to previously studied natural and synthetic examples of these phases. NMR and XAFS data indicated that high-Al proto-imogolite allophanes were similar in structure to imogolite but were less well ordered, and supported the proposed nanoball structures based on rolled octahedral Al sheets. Increasing Si content in allophane produced increasing tetrahedral Al substitution as well as polymerized Si chain structures at Al-Si mole ratios of 1:1, and sheets and possible framework structures at Al-Si mole ratios of 1:2. Fe in allophanes and imogolites substituted exclusively for octahedral Al.

Reflectance spectra of the synthetic allophanes and imogolites were comparable to previously analyzed samples. Variations in Fe content of allophane and imogolite resulted in some observable changes in visible/near-infrared (VNIR) reflectance spectra, but these changes

42 were not detectable in emission spectra. Emission spectra of the samples suggest that variations  
43 in Al-Si ratio of allophanes should be detectable using remotely sensed data. Because allophanes  
44 with different Al-Si ratios typically form in very different environments, this could be significant  
45 for interpretation of formation conditions on Mars, with high-Al compositions suggesting  
46 possible tephra weathering and high-Si compositions indicating possible formation from thermal  
47 waters.

48

49

## Introduction

50 Poorly crystalline aluminosilicates such as allophane and imogolite have been identified  
51 on Mars using orbital infrared spectroscopy (Rampe et al. 2012; Weitz et al. 2014; Bishop and  
52 Rampe 2016). The presence of these nanophase (np) materials on Mars likely indicates a time  
53 when water was intermittent and/or too cold for formation of crystalline clays (Bishop et al.  
54 2018). Analysis of Mars Global Surveyor (MGS) Thermal Emission Spectrometer (TES) data  
55 (Christensen et al. 2001) provided global maps of regions dominated by basaltic and andesitic or  
56 altered terrains (Bandfield et al. 2000; Wyatt and McSween Jr 2002). As spectral libraries of Si-  
57 rich alteration products were developed, TES analyses were extended to include more complex  
58 components including poorly crystalline Si-rich materials (Michalski et al. 2005; Michalski et al.  
59 2006; Rogers and Christensen 2007; Ruff and Christensen 2007; Rampe et al. 2012).

60 Gusev crater contains regions high in Si at Home Plate attributed to opal or hydrated  
61 silica (Squyres et al. 2008; Rice et al. 2010; Ruff et al. 2011). Additional observations of  
62 amorphous Si on Mars were made from orbit using visible/near-infrared (VNIR) Compact  
63 Reconnaissance Imaging Spectrometer for Mars (CRISM) data (Murchie et al. 2009) at Valles  
64 Marineris (Milliken et al. 2008), Nili Fossae (Ehlmann et al. 2009), Nili Patera (Skok et al.  
65 2010), and Mawrth Vallis (Bishop et al. 2008). The Mars Exploration Rovers (MERs), Spirit and  
66 Opportunity, analyzed fine surficial material at Gusev (Spirit) and Meridiani (Opportunity) with  
67 many instruments, and the Mössbauer spectrometer detected the presence of nanophase ferric  
68 oxides, hydroxides, or oxyhydroxides (np-FeOx) (Klingelhöfer et al. 2004; Morris et al. 2004;  
69 Morris et al. 2006a; Morris et al. 2006b). This is consistent with previous VNIR detections of np-  
70 FeOx on Mars (Singer 1982; Bell et al. 1990; Morris and Lauer 1990).

71 An X-ray amorphous component was identified by the Chemistry and Mineralogy  
72 instrument (CheMin) on board the Mars Science Laboratory (MSL) rover at Gale crater (Blake et  
73 al. 2013) that represents ~20-70 wt.% of martian surface material everywhere CheMin has  
74 investigated (Blake et al. 2013; Vaniman et al. 2014; Bristow et al. 2018; Morrison et al. 2018).  
75 The amorphous component most likely represents a combination of volcanic glass and hydrated  
76 amorphous alteration products that are composed primarily of Si, Fe, and S (Ming et al. 2014;  
77 Vaniman et al. 2014). Rampe et al. (2012) identified 10-20% allophane and/or amorphous silica  
78 at North Acidalia, Solis Planum, Sinus Meridiani, and Aonium-Phruxi using TES data. Bishop  
79 and Rampe (2016) found 10-30% allophane (or related phases) in phyllosilicate-rich outcrops at  
80 Mawrth Vallis using a combination of TES and CRISM data. The elevated allophane detections  
81 in the northern plains (Rampe et al. 2012) could be related to observations of leached basaltic  
82 glass in this region (Horgan and Bell 2012). Thus, allophane and imogolite could be a common  
83 component of the martian surface where water was present. Further, they may indicate periods of  
84 cyclical climate change. Progressive cooling and drying of the surface would result in conditions  
85 favorable for amorphous material production, where surface water was not present long enough  
86 or conditions were not warm enough to form more long-range ordered clays (Bishop and Rampe  
87 2016).

88 Characterization of these materials in the lab is essential for increasing spectral  
89 recognition capacities on Mars. Np-aluminosilicates adsorb water readily (Bishop et al. 2013)  
90 and can bind with Fe and other species (Baker et al. 2014; Rampe et al. 2016). Understanding the  
91 relationship between Al-Si-Fe abundance in poorly crystalline aluminosilicates and their spectral  
92 properties will enable future detection of these important materials that encompass up to 70 wt.%  
93 of the surface material investigated by Curiosity at Gale crater. The purpose of this study is to

94 characterize several Fe-bearing allophane and imogolite samples with multiple spectroscopic  
95 techniques to enable more precise detection and characterization of the poorly crystalline  
96 components of the martian regolith.

97

## 98 **Background**

99 Allophanes are poorly crystalline nanoscale aluminosilicates that are prevalent in soils  
100 formed from volcanic ash, where an excess of Si and Al exist in solution (Parfitt 2009). They are  
101 frequently found in association with imogolite, most commonly as products of the weathering of  
102 volcanic tephra. Allophane imparts unique chemical and physical properties to soils in which it is  
103 a predominant mineralogical component, and those properties have implications for the content  
104 and retention of phosphate, sulfate, and H<sub>2</sub>O in such soils (Rajan 1979; Rampe et al. 2016).

105 Allophane and imogolite exhibit rolled morphologies (Figure 1) with nanometer-scale  
106 diameters (Abidin et al. 2007), and therefore lack the long-range ordered orthogonal lattices  
107 observed in macroscopically crystalline materials, although imogolite exhibits long-range order  
108 in one direction. Allophane and imogolite are difficult to characterize due to their small size and  
109 lack of macroscopic crystal ordering; however, research has illuminated much about their  
110 structure and formation (Henmi and Wada 1976; Farmer et al. 1980; Abidin et al. 2007; Abidin  
111 et al. 2008; Creton et al. 2008b; Creton et al. 2008a; Parfitt 2009; Bishop et al. 2013; Baker et al.  
112 2014).

113 Imogolite exhibits nanotubular morphology (Cradwick et al. 1972; Abidin et al. 2007).  
114 Nanotubes are typically 2 nm in exterior diameter and the strands may be tens of nanometers in  
115 length. These tubes are thought to consist of a rolled gibbsite-like sheet of octahedrally

116 coordinated Al with isolated silicon tetroxide tetrahedra bonded to the tube interior to yield an  
117 overall molar Al:Si ratio of 2:1 (Cradwick et al. 1972). Each orthosilicate unit is bonded to three  
118 Al atoms and no silica polymerization is observed. Because of its tubular morphology, imogolite  
119 has no long-range structure in the cross-tube direction but does possess long-range structure in  
120 the along-tube direction. Computer modeling has confirmed this structure and reproduced the X-  
121 ray diffractogram of natural imogolite samples (Guimarães et al. 2007; Creton et al. 2008b). In  
122 synthesis experiments, imogolite-like aluminogerminates have been observed to evolve from  
123 nanospherical allophane-like structures upon aging for periods of >2 weeks (Levard et al. 2010).

124         Due to the lack of long-range crystallographic order, allophanes have been difficult to  
125 characterize by X-ray diffraction (Parfitt 2009), and most of the information known about their  
126 chemical structures has been determined by methods such as infrared spectroscopy, X-ray  
127 absorption spectroscopy (XAS), and nuclear magnetic resonance (NMR), and by computer  
128 modeling.

129         Natural allophanes display a continuous variation in Al:Si ratio. High-Al or proto-  
130 imogolite allophane exhibits a molar Al:Si ratio of approximately 2:1. Allophanes with higher Si  
131 contents have molar Al:Si ratios as low as 0.9 (Parfitt 2009). The lowest Al:Si ratios are found in  
132 “stream-deposit” allophanes that precipitate from silica-saturated stream or spring water (Wells  
133 et al. 1977; Childs et al. 1990; Parfitt 1990).

134         Proto-imogolite allophane is thought to have a hollow, nanospherical structure that is  
135 similar in cross section to the cross-tube structure of imogolite (Figure 1). In the proposed  
136 structure, an exterior gibbsite-like sheet of octahedrally coordinated Al is rolled into a nanoball  
137 of diameter 3.5–6 nm. Orthosilicate units are bonded to the nanoball interior as in the structure of  
138 imogolite. Computer modeling suggests that four to six pores are present in the nanoball

139 structure (Abidin et al. 2007; Creton et al. 2008a). NMR and Fourier transform infrared  
140 spectroscopy analyses suggest that high-Si allophanes formed in soil environments have a similar  
141 fundamental structure to high-Al allophanes, and that the additional silica is accommodated in a  
142 polymerized form in the nanoball interior (Parfitt 1990). In highly Si-enriched “stream deposit”  
143 type allophanes, the framework is proposed to be a nanospherical shell of polymerized Si, with a  
144 partial or fragmental octahedral Al ( $Al_O$ ) shell and with some Al substitution in tetrahedral sites  
145 ( $Al_T$ ) (Childs et al. 1990). The tetrahedral Al substitution in these high Si species follows  
146 Lowenstein’s rule for zeolites where no Al-O-Al linkages are allowed, resulting in a constant  
147  $Al_T:Si$  of 1:3 (Childs et al. 1990). An alternative structure for Si-rich allophane based upon a  
148 curved kaolinite structure containing a defective tetrahedral sheet was proposed by MacKenzie et  
149 al. (1991). At present, no apparent consensus exists on whether high-Si and high-Al forms of  
150 allophane represent fundamentally different types of structures, or whether they represent a  
151 single fundamental structural type that is progressively modified to accommodate varying Al:Si  
152 ratios.

153 Fe-substituted natural and synthetic allophane and imogolite samples have been described  
154 and analyzed using a variety of techniques (Kitagawa 1973; Horikawa and Soezima 1977;  
155 McBride et al. 1984; Baker and Strawn 2012). These studies found that Fe in allophane and  
156 imogolite was spectrally distinct from Fe in Fe oxides, hisingerite and nontronite. Most Fe was  
157 substituted for Al in octahedral coordination (Figure 1), although some Fe in natural allophane  
158 and imogolite samples may be present as a separate ferrihydrite phase (Baker et al. 2014).  
159 Substitution of Fe into the structures of np-aluminosilicates has been reported to affect their  
160 morphology (Joussein et al. 2005), as well as the kinetics and end products of their ripening to  
161 more crystalline clay minerals (McBride et al. 1984; Farmer et al. 1991; Farmer 1997). Fe-



162 substituted allophanes may ripen to an Fe-depleted phase plus ferrihydrite (McBride et al. 1984),  
163 or they may recrystallize to Fe-bearing clays such as nontronite (Farmer et al. 1991) or  
164 ferruginous beidellite (Farmer 1997). The specific conditions that lead Fe-bearing allophane to  
165 ripen into various end products are not well understood.

166 The objectives of the present study were: (1) to investigate Fe speciation and  
167 coordination state in synthetic allophane and imogolite samples, and (2) to examine how the  
168 allophane and imogolite structures are affected by variations in Al:Si and by isomorphic  
169 substitution of Fe for Al. We used spectroscopic data and structural modeling to test existing  
170 models of allophane structure, to examine the hypothesis that high-Al and high-Si forms of  
171 allophane have the same fundamental structure, and to determine whether the presence of  
172 isomorphically substituted Fe affects these structures. A further objective was to characterize the  
173 reflectance and emission spectra of these materials in support of remote identification of them on  
174 Mars and other planetary bodies.

## 175 **Methods**

### 176 **Materials Synthesis**

177 A suite of synthetic Fe-bearing and Fe-free allophane samples was created using the  
178 method described by Baker and Strawn (2012) that was modified from Montarges-Pelletier et al.  
179 (2005). A solution of 0.1 M  $\text{AlCl}_3$  was mixed with a sufficient amount of tetraethyl orthosilicate  
180 (TEOS) to obtain the desired Al:Si ratio for each allophane sample synthesized (Table 1). Fe-  
181 substituted allophanes were produced by mixing 0.1 M  $\text{FeCl}_3$  with the  $\text{AlCl}_3$  solution (replacing  
182 some of the  $\text{AlCl}_3$  with  $\text{FeCl}_3$  in order to maintain constant total volume of 0.1 M chloride  
183 solution and correct allophane-forming stoichiometry), to produce the desired Fe content and

184 (Al+Fe):Si ratio. A solution of 0.1 M NaOH was titrated into this mixture under constant stirring  
185 in a N<sub>2</sub> purged bottle. Typical synthesis volumes were 250 mL of AlCl<sub>3</sub> + FeCl<sub>3</sub> and 750 mL of  
186 NaOH plus the volume of TEOS needed to obtain the desired Si content. At the end of the  
187 titration, the final solution pH was recorded. The resulting suspension of gel in supernatant was  
188 stirred for 24 hours, then heated to 95 °C for five days. The suspension was centrifuged to  
189 separate the gel, which was placed in dialysis tubing and dialyzed against flowing DI water to a  
190 conductivity less than 5 μS/cm. A sample of the centrifuged supernatant was filtered through a  
191 0.45 μm filter, acidified, and refrigerated for analysis. A subsample of each synthesized gel was  
192 stored frozen. The remainder of each gel was freeze-dried for analysis.

193 Under oxygen-free martian conditions, allophanes may form in an environment where Fe  
194 is present as Fe<sup>2+</sup>. Samples were therefore also synthesized using Fe<sup>2+</sup> by replacing the FeCl<sub>3</sub> in  
195 the synthesis procedure with FeCl<sub>2</sub>. These syntheses produced gels that were green in color,  
196 suggesting that Fe in them may have remained divalent. However, a color change from green to  
197 brown during dialysis and freeze drying suggested that Fe<sup>2+</sup> in the gel samples began to oxidize  
198 rapidly upon exposure to air. Therefore, the only samples that appeared to retain unoxidized Fe  
199 were those preserved as frozen gels. As a result, analyses requiring dried samples could not be  
200 performed on confirmed Fe(II)-bearing allophanes. Of the following sample analysis techniques,  
201 only X-ray absorption spectroscopy permitted analysis of a hydrated gel sample that retained  
202 some Fe(II). Previous studies using allophanes synthesized using the same techniques showed  
203 that the XAFS spectra of the same samples in both hydrated gel form and as freeze-dried  
204 powders yielded identical spectra and modeling results (Baker et al. 2014).

205 A suite of synthetic Fe(III)-bearing and Fe-free imogolite samples was synthesized by Z.  
206 Abidin using a previously established method (Abidin et al. 2008). Imogolite suspensions

207 produced using this synthesis were shipped to the University of Idaho where they were freeze-  
208 dried for analysis.

209 All synthesized samples were analyzed by X-ray diffractometry (XRD) to confirm that  
210 they contained no crystalline materials. In all samples, broad, poorly defined peaks were present  
211 at  $2\theta$  of  $12^\circ$  and  $26^\circ$ .

### 212 **Inductively Coupled Plasma Atomic Emission Spectroscopy**

213 All supernatant solutions from synthesis experiments were analyzed on a ThermoFisher  
214 iCAP Duo inductively-coupled plasma atomic emission spectrometer (ICP-AES) to verify  
215 synthesized compositions. Samples were analyzed for Fe, Al and Si. Calibration solutions, a  
216 blank and a quality control solution were mixed using 0 ppm, 10 ppm and 50 ppm concentrations  
217 of proposed analytes with small additions of  $\text{HNO}_3$  and HCl to match preservation methods of  
218 supernatants. ICP results were used to calculate the true anhydrous formula of the synthesis  
219 products by difference from the composition of the original starting solutions.

### 220 **Diffuse Reflectance Infrared Spectroscopy**

221 Fourier transform infrared (FTIR) spectroscopic analyses were carried out on a Perkin-  
222 Elmer System 2000 (Thermo Scientific, Waltham, Massachusetts, USA), using a mixture of 3  
223 wt.% sample in optical-grade KBr that was placed into a steel sample cup and analyzed in a  
224 diffuse reflectance mounting geometry. Samples were scanned 100 times and the spectra were  
225 averaged. Spectra were recorded from  $4000$  to  $600\text{ cm}^{-1}$  using  $1\text{ cm}^{-1}$  resolution and processed  
226 using the Kubelka-Munk algorithm provided in Perkin Elmer Spectrum 2.0 software. Peak fitting  
227 for these spectra was performed in Origin Pro 2019a using the Peak Analyzer tool.

### 228 **Reflectance Spectroscopy of Bulk, Particulate Samples**

229 Bidirectional reflectance spectra were measured of bulk (unmixed with KBr or other  
230 compounds), particulate samples from 0.3-2.5  $\mu\text{m}$  under ambient conditions at Brown  
231 University's RELAB using a bidirectional VNIR spectrometer relative to Halon and a biconical  
232 Nicolet FTIR spectrometer in a controlled, dry environment relative to a rough gold surface as in  
233 previous studies (Bishop et al. 2013). The bidirectional spectra were acquired from 0.3 to 2.5  $\mu\text{m}$   
234 at 5 nm spectral sampling. FTIR reflectance spectra were measured under dry conditions from 1-  
235 50  $\mu\text{m}$  and then scaled to the bidirectional data near 1.2  $\mu\text{m}$  to create composite, absolute  
236 reflectance spectra.

### 237 **Thermal Emission Spectroscopy of Particulate Samples**

238 Thermal emissivity spectra of particulates compressed into pellets were measured at the  
239 ASU Mars Space Flight Facility using a modified Nicolet Nexus 670 FTIR interferometric  
240 spectrometer. Spectra were measured 270 times over ~4 minutes over the range of 2000 to 200  
241  $\text{cm}^{-1}$  (5-50  $\mu\text{m}$ ) with 2  $\text{cm}^{-1}$  spectral sampling as in previous studies (Ruff et al. 1997; Rampe et  
242 al. 2012). Pellets were measured in copper sample cups painted black so that they behave as a  
243 blackbody and heated to 80  $^{\circ}\text{C}$  before and during data collection. Blackbodies at 70 and 100  $^{\circ}\text{C}$   
244 were measured before sample measurements to calibrate raw data to radiance (Christensen and  
245 Harrison 1993).

### 246 **$^{27}\text{Al}$ and $^{29}\text{Si}$ Magic Angle Spinning Nuclear Magnetic Resonance**

247 Samples of Fe-free synthetic allophanes and imogolites were analyzed using  $^{27}\text{Al}$  and  $^{29}\text{Si}$   
248 magic angle spinning (MAS) solid-state nuclear magnetic resonance spectroscopy (NMR) on a  
249 Bruker AVANCE 500 MHz spectrometer (Bruker Biospin, Rheinstetten, Germany). Samples

250 were spun at 12.6 kHz and were allowed to run until a signal to noise ratio of greater than 500  
251 was achieved. Samples containing Fe were not run due to their paramagnetic nature.

## 252 **X-Ray Absorption Spectroscopy (XAFS)**

253 Bulk Fe K- edge X-ray absorption near edge spectroscopy (XANES) and extended fine  
254 structure spectroscopy (EXAFS) analyses of Fe-bearing samples were performed at beamline 7-3  
255 of the Stanford Synchrotron Radiation Laboratory (SSRL). Beamline 7-3 is fed by the SPEAR  
256 ring operating with a beam current of 500-495 mA. The X-rays are diverted using a 20 pole 2-  
257 tesla wiggler source, then through a vertical collimating mirror into the monochromator. The  
258 monochromator for this beamline is two parallel Si(220) crystals with a 6-mm entrance slit. This  
259 experimental setup results in a spot size of approximately 3 x 15 mm. A Lytle fluorescent ion  
260 chamber detector was used to collect fluorescence measurements over the entire Fe K-edge  
261 EXAFS energy range of 6880-7873 eV with an energy step size of 0.35eV. All spectra were  
262 collected at 10 K using a liquid He cryostat to prevent beam damage and scanned 4-12 times to  
263 increase the signal to noise ratio. Allophane and imogolite samples, in the form of either wet gels  
264 or dry powders, were packed into aluminum sample holders 0.7-mm thick and held in place with  
265 Kapton tape. No differences are observed between wet gel and dry powder packed mounts of the  
266 same synthetic sample (Baker et al. 2014). In general, allophane samples were analyzed as gels  
267 and imogolite as dried powders, but for lower-Fe allophanes, the higher Fe concentration in the  
268 dried samples yielded improved data in the form of a better signal to noise ratio. The multiple  
269 scans were calibrated to an Fe foil, and merged and processed using Athena (Ravel and Newville  
270 2005).

## 271 **FEFF Modeling**

272 The merged spectra were normalized and background subtracted using a cubic spline.

273 The fitting strategy used in this study follows the approach described by Baker and Strawn  
274 (2012) and Baker et al. (2014) in previous studies of Fe in clay minerals.

275 Shell fitting of the allophane samples was carried out using the 5-shell allophane nanoball  
276 model as well as a 5-shell dioctahedral smectite model, following the modelling philosophy of  
277 Baker et al. (2014). A detailed description of these models may be found in that work; the most  
278 significant difference between the two is in the Si backscattering shell. Atomic coordinates for  
279 the smectite model were taken from Tsipursky and Drits (1984) and coordinates for the nanoball  
280 model were taken from a section of the model nanoball described by Creton et al. (2008a). Paths  
281 were generated from the atomic coordinates using Atoms (Ravel 2001) and shell fitting was  
282 carried out using Artemis (Ravel and Newville 2005).

283 In conducting the fitting, all path lengths were optimized at first, and were then  
284 constrained to be equal within that fit. Fe-O3 shell distances were fixed for all models except the  
285 1:1 Fe(III) smectite model, where allowing it to float resulted in a better fit. Debye-Waller  
286 EXAFS factors were optimized for the first Fe-O1 shell and fixed to be equal to the former for  
287 the Fe-Fe, Fe-Al, and Fe-Si backscattering paths. Debye-Waller EXAFS factors were also  
288 optimized for the Fe-O2 and then fixed to be equal for the Fe-O3 shell. Octahedral sites were  
289 fitted with either Fe or Al, with the total number of Fe-Metal backscatterers constrained to sum  
290 to three, resulting in a dioctahedral sheet. Trioctahedral fits, where Fe-metal backscatters sum to  
291 6, were attempted for the Fe(II) substituted samples, but no recognizable improvement in the fit  
292 was observed. The path length was optimized for the Fe-Si backscattering path, with the number  
293 of Si atoms fixed at 2 for the smectite model and 3 for the nanoball model.

294

295

## Results

### 296 Synthetic Allophane

297 The sample compositions span the range of naturally occurring allophanes from high Si  
298 (molar Al:Si 1:2) through halloysite-like (Al:Si 1:1) to proto-imogolite (Al:Si 2:1). These three  
299 Al:Si compositions were synthesized with Fe<sup>3+</sup> isomorphically substituted for 0, 2, 5, and 10  
300 mol.% Al in the sample. This yielded 12 samples of allophane with varying compositions and  
301 physical properties. Previous synthetic work suggested that the amount of Fe that can substitute  
302 in synthetic allophane varies with Si content (Baker et al., 2014). In the present study, however,  
303 allophanes at all three Al:Si ratios were successfully synthesized with Fe isomorphically  
304 substituted for 10% of Al.

305 Results from ICP-AES analyses of residual Si, Al, and Fe contents in supernatant  
306 solutions were used to calculate the true Al:Si ratio and true Fe content of the synthetic samples  
307 by difference from the initial solutions (Table 1). The results indicate that the intended Al:Si  
308 ratios and Fe contents were achieved. Increased Fe content correlated with slight decreases in  
309 bulk Al:Si ratio in the solids, indicating that Fe was substituting for Al in the structure as  
310 expected. Also shown in Table 1 are pseudo-cationic formulas for each synthetic allophane  
311 composition, calculated from the Al, Fe, and Si contents, to allow for easier comparison of  
312 compositional differences between samples.

313 Allophane synthesis was also carried out using Fe(II) rather than Fe(III), to examine  
314 whether Fe substitution into allophane is likely under reducing conditions. Allophanes containing  
315 10% Fe(II) substituted for Al were successfully synthesized at Al:Si ratios of 1:2 and 2:1, but  
316 synthesis at Al:Si of 1:1 was not successful. As noted above, Fe in these samples oxidized

317 rapidly upon exposure to air during processing and freeze-drying. As a result, the only analysis  
318 presented here of an allophane still containing residual Fe(II) is of a 2:1 Al:Si sample that was  
319 stored as a frozen gel, and analyzed as a gel by XAFS spectroscopy. The results of this analysis  
320 are given below.

### 321 **Visible and Infrared Spectroscopy**

322 Infrared spectra of Fe-free synthetic imogolite and allophane samples (Figures 2-6) show  
323 absorption bands that are typical for these materials (Bishop et al. 2013) and provide context for  
324 spacecraft observations. Kubelka-Munk transformed spectra of sample-KBr mixtures are shown  
325 in Figure 2 and provide the strongest absorptions. Mid-IR emissivity spectra of the pressed pellet  
326 samples (Figure 3) are noisier than reflectance spectra, but they are directly comparable to  
327 spacecraft data, whereas the reflectance spectra of particulate samples (Figures 4-5) and  
328 particularly of KBr-sample mixtures (Figure 2) may differ from remotely sensed spectra. The  
329 spectral contrast is relatively low because of the small particle size.

330 Broad H<sub>2</sub>O stretching vibrations are observed between 3400 and 3600 cm<sup>-1</sup>. Imogolite  
331 and high-Al allophane both display a broad hydroxyl band near 3535 cm<sup>-1</sup>, which displays  
332 slightly more structure for imogolite than for high-Al allophane, but the two spectra are  
333 otherwise similar. This band shifts to lower wavenumber with increasing Si content (Figure 2,  
334 vertical solid and dashed lines).

335 The Si-O stretching features at ~950-1050 cm<sup>-1</sup> can be seen in all samples. Imogolite and  
336 high-Al allophane show bands near 935 and 950 cm<sup>-1</sup>, respectively, that are characteristic of the  
337 orthosilicate Si-O-Al stretching vibration in high-Al allophane (Thill 2016); imogolite can  
338 display a doublet in this region, but this synthetic sample does not. The 950 cm<sup>-1</sup> band broadens



339 and shifts to shorter wavelengths with increasing Si content; this likely reflects growth of an  
340 additional Si-O-Si absorption feature near  $1050\text{ cm}^{-1}$  (Parfitt et al. 1980) that results from  
341 increasing abundance of polymerized Si in the allophane structure. Deconvolution of the 800-  
342  $1350\text{ cm}^{-1}$  region of the diffuse reflectance spectrum of the Fe-free 1:2 Al:Si allophane (Figure 2)  
343 yielded a good fit to a primary peak positioned at  $1055\text{ cm}^{-1}$  with subsidiary peaks at 893 and  
344  $1176\text{ cm}^{-1}$  (Figure 6). These shifts in Si-O-Al stretching vibrations are also observable in  
345 emissivity spectra (Figure 3). Few differences are observable between the 1:2 and 1:1 allophane  
346 compositions in emissivity spectra, except that the Si-O-Si stretching feature near  $1045\text{ cm}^{-1}$  is  
347 absent or poorly developed in the 1:2 samples but clearly discernable in the higher-Si 1:1  
348 samples (Figure 3, dashed line at  $1045\text{ cm}^{-1}$ ). The Christiansen feature (reflectance minimum or  
349 emissivity maximum) is observed near  $1215\text{ cm}^{-1}$  for allophane and near  $1150\text{ cm}^{-1}$  for imogolite  
350 and this shifts slightly towards lower wavenumber with increasing Fe in the imogolite sample  
351 (Figure 4, vertical dotted and solid lines and arrow).

352 Al-O-Si deformation and Si-O bending features at  $\sim 400\text{-}600\text{ cm}^{-1}$  can be resolved in the  
353 imogolite spectra (Figure 4). OH out-of-plane bending modes occur near  $610\text{ cm}^{-1}$  for allophane  
354 and at  $595\text{ cm}^{-1}$  for imogolite (Bishop et al. 2013); the  $595\text{ cm}^{-1}$  feature is observed in both the  
355 imogolite and allophane emissivity spectra shown in Figure 3 but no feature is apparent at  $610$   
356  $\text{cm}^{-1}$  (dotted lines). The lack of the OH out-of-plane banding mode in allophane may result from  
357 the presence of defects in the structure of proto-imogolite-like compounds, as suggested by the  
358 weak Al(IV) and Al(V) peaks observed in NMR. The presence of these compounds or defects  
359 may disrupt the short-range order of allophane and degrade its resulting emissivity spectra.  
360 Features due to Si-O-Al bending vibrations were observed at 545, 420 and  $335\text{ cm}^{-1}$  for

361 allophane and at 495, 415, and 335  $\text{cm}^{-1}$  for imogolite by Bishop et al. (2013). Similar bands are  
362 observed in this study (Figure 4a, dotted vertical lines).

363 The position of the Si-O-Al stretching band shifts slightly toward lower wavenumbers in  
364 the imogolite mid-IR reflectance spectra with increasing Fe (Figure 4a, vertical line and arrow).  
365 In contrast, the Si-O-Al bending bands near 495 and 415  $\text{cm}^{-1}$  appear to shift towards higher  
366 wavenumbers with increasing Fe in these spectra (Figure 4a, vertical line and arrow). The Fe-  
367 bearing allophane spectrum includes a doublet band for the Si-O-Al stretching vibration centered  
368 near 1025 and 950  $\text{cm}^{-1}$  (Figure 4b, vertical solid and dotted lines). These shifts, however, are  
369 relatively small and are not observed in thermal-IR emissivity spectra.

370 Reflectance bands for Fe-free allophane and imogolite in the mid-IR range (Figure 4)  
371 were also comparable to previous measurements on natural and synthetic allophane and  
372 imogolite samples (Bishop et al. 2013; Weitz et al. 2014). The addition of Fe in these materials  
373 resulted in overall darkening of the samples (Figure 4). Spectra in the VNIR range (Figure 5)  
374 show the development of electronic transition bands from Fe near 0.45 and 0.9  $\mu\text{m}$  (dashed  
375 lines). Fe-free allophane spectra display a doublet near 1.38 and 1.40  $\mu\text{m}$  from  $\text{OH}_{2\nu}$  (OH  
376 stretching overtones), a band at 1.92  $\mu\text{m}$  from  $\text{H}_2\text{O}_{\nu+\delta}$  (bending and stretching  $\text{H}_2\text{O}$  combination  
377 band), and a band at 2.19  $\mu\text{m}$  from  $\text{OH}_{\nu+\delta}$  (bending and stretching OH combination band),  
378 consistent with previous work (Bishop et al., 2013). Fe-free imogolite has similar bands as  
379 allophane, but the doublet from  $\text{OH}_{2\nu}$  occurs at 1.37 and 1.39  $\mu\text{m}$ , as reported by Bishop et al.  
380 (2013). The addition of Fe to the structures of allophane and imogolite did not significantly  
381 affect the position and breadth of the OH and  $\text{H}_2\text{O}$  overtone and combination bands near 1.4, 1.9,  
382 and 2.2  $\mu\text{m}$ . However, Fe in the structures of allophane and imogolite appears to increase the  
383 intensity of the OH stretching overtone at  $\sim 1.37\text{-}1.38 \mu\text{m}$ , such that the band at 1.38  $\mu\text{m}$  becomes

384 more intense than the 1.40  $\mu\text{m}$  band in the spectrum of 1:1 allophane with 10% Fe. A similar  
385 effect is observed for the spectrum of imogolite with 5% Fe compared to the Fe-free sample.  
386 Subtle broadening of these spectral features is observed for the Fe-enriched samples, but this  
387 effect is only barely noted in lab spectra and would not be detectable in remote sensing studies.  
388 The addition of Fe to the structures of allophane and imogolite did not significantly affect the  
389 position and breadth of the OH and H<sub>2</sub>O stretching and bending vibrations at  $\sim$ 1.4, 1.9, and 2.2  
390  $\mu\text{m}$ . Fe in the structures of allophane and imogolite appears to increase the intensity of the first  
391 OH bending overtone at  $\sim$ 1.38  $\mu\text{m}$ , where, in the spectrum of 1:1 allophane, the band at 1.38  $\mu\text{m}$   
392 becomes more intense than the 1.40  $\mu\text{m}$  band with 10% Fe

393         Addition of Fe(III) to the allophane structure resulted in increased amplitude of the  
394 diffuse reflectance bands (Figure 2), although this was less evident in the allophane with 1:1  
395 Al:Si than in either the high-Al or high-Si compositions. Substitution of Fe(II) into allophane,  
396 however, did not alter the diffuse reflectance spectrum in any observable way, although this  
397 could be because Fe in the sample was oxidized during freeze-drying. No obvious Fe-Al-OH or  
398 Fe-Fe-OH bands were resolvable in the spectra, even for the highest-Fe samples.

### 399 <sup>27</sup>Al MAS NMR

400         The relative abundances of four-coordinate (Al<sub>T</sub>), five-coordinate (Al<sub>P</sub>) and six-  
401 coordinate Al (Al<sub>O</sub>) in the allophane structure can be quantified by integration of the peak  
402 curves. The peaks are located at  $\sim$ 10,  $\sim$ 36, and  $\sim$ 60 ppm for Al<sub>O</sub>, Al<sub>P</sub>, and Al<sub>T</sub>, respectively  
403 (Figure 7). One peak, corresponding to Al<sub>O</sub>, is predominant in imogolite. Two distinct peaks are  
404 observed in the allophane spectra, corresponding to Al<sub>O</sub> and Al<sub>T</sub>. Virtually all Al in imogolite is  
405 six-coordinate, whereas high-Al “proto-imogolite” allophane contains a small proportion of Al<sub>T</sub>  
406 ( $\sim$ 6%) and Al<sub>P</sub> ( $\sim$ 3%). The total percentage of tetrahedrally coordinated Al in the structure

407 increases linearly with increasing Si content (Table 1) but is higher in proto-imogolite allophane  
408 than in imogolite although the two compounds have the same nominal Al:Si ratio.

#### 409 **<sup>29</sup>Si MAS NMR**

410 Unlike the large shifts seen in the Al NMR spectra, which correlate to Al coordination  
411 number, small shifts seen in the peak differentiation in the Si NMR data are strongly correlated  
412 to Si polymerization (Figure 8), and therefore indirectly to the number of Si-Al neighbors in the  
413 structure. Imogolites exhibit a spectrum with a well resolved peak at ~79 ppm that arises from  
414 the presence of orthosilicate. Proto-imogolite allophanes exhibit a peak in the same location that  
415 is broader, suggesting minor polymerization of Si in this sample despite its relatively low Si  
416 content. As Si is introduced into the structure, a second, poorly resolved, broad peak develops  
417 that is centered between -86 and -90 ppm for the 1:1 Al:Si sample and at ~100 ppm for the 1:2  
418 Al:Si sample. This peak dominates the spectrum of the 1:2 Al:Si sample, with only a poorly  
419 defined remnant peak remaining near 80 ppm, whereas the two peaks have similar magnitude in  
420 the 1:1 Al:Si sample. We interpret the peak between -86 and -90 ppm as arising from Q2 chain  
421 silicate structures, whereas the peak near -100 ppm is consistent with Q3 sheet silicate structures.  
422 These results suggest that the 1:1 Al:Si allophane contains some orthosilicate tetrahedra as well  
423 as some polymerized Si chains, and are consistent with a model for this composition of a proto-  
424 imogolite-like structure with additional polymerized Si in its interior. The 1:2 Al:Si sample, by  
425 contrast, shows little evidence for orthosilicate tetrahedra and its spectrum is consistent with a  
426 phyllosilicate-like structure or a rolled tetrahedral sheet.

#### 427 **XANES and EXAFS spectra**

428           The near-edge X-ray absorption spectra are typical of previous analyses of Fe-substituted  
429 allophanes (Baker and Strawn 2012; Baker et al. 2014), except for the Al:Si 2:1, 10% Fe(II)-  
430 substituted sample. That sample displays a shift to lower energy of approximately 1 eV in the  
431 absorption edge (Figure 9a, arrow), indicating that some Fe(II) remained in the sample; this shift  
432 is more easily observable in the first derivative of the spectrum (Figure 9b, arrow). The pre-edge  
433 peak is also shifted approximately 0.3 eV lower in energy, to 7113.2 eV. The pre-edge and edge  
434 positions for this spectrum suggest that, even in this sample, much of the Fe was oxidized to  
435 Fe(III) and only some has been retained as Fe(II). The other Fe(II) substituted sample, at Al:Si of  
436 1:2, displays no edge shift to lower energy, indicating the Fe in this sample all oxidized to  
437 Fe(III).

438           The XANES data support the conclusion that Fe is isomorphically substituting for Al in  
439 octahedral coordination, and that tetrahedral substitution of Fe for Si is not significant in the  
440 samples studied. The presence of tetrahedral Fe, or of Fe in (oxyhydr)oxide phases, results in  
441 enhanced amplitude of the pre-edge XANES peak (Baker and Strawn 2012; Baker et al. 2014),  
442 which is not observed in the spectra presented here (Figure 9).

443           EXAFS spectra and Fourier transformed spectra of the synthetic Fe(III) substituted  
444 allophanes and imogolite (Figure 10) are similar to previously published spectra (Baker and  
445 Strawn 2012; Baker et al. 2014) but with greater development of the features that are  
446 characteristic of Fe-Fe next neighboring atoms. These features include the peaks in the  $\chi$   
447 spectrum near 5 and 7.25  $\text{\AA}^{-1}$  and the peak centered near 2.8  $\text{\AA}$  in the Fourier transformed  
448 spectrum. The high-Si allophane sample composition showed weaker development of the Fe-Fe  
449 next neighbor features than did higher-Al compositions. Although the sample Al:Si ratios are not  
450 exactly the same, this observation is in agreement with that of Baker et al. (2014). The spectrum

451 of the high-Si, Fe(II) substituted allophane shows very little development of the characteristic  
452 Fe-Fe features. This spectrum is characteristic of Fe in octahedral coordination but with almost  
453 all Fe-Al next neighbors rather than Fe-O-Fe bonds. The spectrum of the high-Al, Fe(II)  
454 substituted allophane, by contrast, is very similar to that of the Fe(III) substituted allophane, even  
455 though this sample is shown by the XANES spectrum to contain some Fe(II).

## 456 **EXAFS Modeling**

457 Model fits, coordination numbers, path lengths, and Debye-Waller factors for Fe<sup>3+</sup>  
458 substituted samples are summarized in Table 2. Modeled Fe-Fe coordination numbers for Fe(III)  
459 substituted samples (Table 2) using the nanoball model are highest with high Al content and  
460 lowest in the high-Si sample containing Fe(II). Fe-O1 path lengths exhibit very similar values for  
461 all samples, ranging from 1.97 to 1.99. Fe-Fe1 path lengths range from 3.00 to 3.06 Å, while Fe-  
462 Al path lengths range from 2.99 to 3.04 Å. Fe-Si path lengths cluster between 3.24 and 3.28 Å.  
463 Path lengths do not differ significantly between Fe(II) and Fe(III) substituted samples.

464 Fe-Fe coordination numbers for Fe substituted samples calculated using the smectite  
465 model are higher in all cases than those calculated using the nanoball model. Overall patterns  
466 among path lengths are similar to the nanoball model. Fe-Fe path lengths range from 3.03 to 3.08  
467 Å, and Fe-Al path lengths range from 3.01 to 3.06 Å. Fe-Si path lengths cluster between 3.23 and  
468 3.28 Å. Path lengths do not differ significantly between Fe(II) and Fe(III) substituted samples.

469 The Fe-Fe coordination number calculated for the Fe(II) substituted high-Si allophane  
470 was much lower than CNs calculated for any other sample. This is consistent with the  
471 observation above that typical Fe-Fe next neighbor features are poorly developed in the spectrum  
472 of this sample.

473

## Discussion

### 474 **Chemical substitution patterns among allophanes and imogolites**

475 Comparison of  $^{27}\text{Al}$  NMR data with ICP-AES data (Table 1) shows that the  $\text{Al}_T:\text{Si}$  ratio  
476 of higher-Si allophanes stays constant at  $\sim 1:3$ , consistent with naturally occurring high Si  
477 allophanes (Childs et al. 1990; Ildefonse et al. 1994). This ratio also follows Loewenstein's rule  
478 for zeolites, which states that no Al-O-Al linkages are allowed within the tetrahedral sheet due to  
479 charge imbalances (Loewenstein 1954). This represents a tetrahedral Si sheet containing  
480 substituted  $\text{Al}_T$  tetrahedra, with no  $\text{Al}_T$  tetrahedra sharing edges. This is consistent with the  
481 results of  $^{29}\text{Si}$  NMR (Figure 8) indicating sheet silicate structures were present in the high-Si  
482 allophane. Previous work suggested that natural high-Si allophanes from Silica Springs have a  
483 structure that is based on a silicate sheet comparable to that in muscovite mica, rolled into a  
484 sphere with an external tetrahedral layer, with an incomplete octahedral sheet in the nanosphere  
485 interior (Childs et al. 1990). The results presented here suggest that synthetic high-Si allophanes  
486 have a similar structure to naturally occurring ones.

487 The  $\text{Al}_T:\text{Si}$  ratio of high-Al allophane is 0.13, half that of the more Si-rich allophanes.  
488 This is in accordance with the  $^{29}\text{Si}$  NMR spectrum of this material (Figure 8) which shows that it  
489 contains relatively little polymerized silica. This sample does contain more polymerized Si than  
490 the imogolite samples, however (Figure 8). It also contains a small proportion of  $\text{Al}_V$ , whereas  
491 imogolite contains very little (Figure 7). These observations from NMR indicate that the proto-  
492 imogolite allophanes contain more structural defects than the imogolites that they  
493 compositionally resemble. This likely results from the deformations necessary to form a  
494 nanosphere, as opposed to a nanotube, from a rolled sheet structure.

495 Previous results from Fe K-edge EXAFS spectroscopy of synthetic allophanes (Baker  
496 and Strawn 2012; Baker et al. 2014) found that all Fe present in the samples was in octahedral  
497 coordination. They interpreted these results as not supporting the model proposed by Childs et al.  
498 (1990) for the structure of higher-Si allophanes because that model calls for incomplete  
499 octahedral sheets, and no evidence was found for Fe in other than full octahedral coordination.  
500 Incomplete octahedral sheets would be lined along the sheet edges with defect sites occupied by  
501 cations that were not in full octahedral coordination. In particles containing only a few hundred  
502 octahedral cations (e.g. Creton et al. (2008a)), the cations along the edges of incomplete sheets  
503 would represent a significant fraction of total octahedral cations, and would likely be detectable.  
504 The present study includes similar observations of Fe coordination but suggests that the previous  
505 interpretation by Baker and Strawn (2012) and Baker et al. (2014) was not correct. The <sup>29</sup>Si  
506 NMR and FTIR results indicate that polymerized Si is present in the high-Si allophane samples,  
507 supporting the formation of a phyllosilicate-like structure. Bulk chemistry of the samples  
508 indicates that there is not sufficient Al (+ Fe) present in the solid to form a complete octahedral  
509 sheet in a nanoball structure based on tetrahedral Si. In addition, the <sup>27</sup>Al NMR data for the Al:Si  
510 1:2 sample shows that nearly half of the Al present in the samples is in tetrahedral coordination,  
511 so the ratio of tetrahedral (Si + Al) to octahedral Al in this sample is approximately 4:1.  
512 However, Fe K-edge XANES and EXAFS data still indicate that Fe is in octahedral coordination  
513 in high-Si allophane samples. Both XANES / EXAFS data and bulk compositional data indicate  
514 that Fe is substituting for Al rather than being present in a separate (oxyhydr)oxide phase. This  
515 suggests that Fe substituted into the allophane structure may only occupy non-edge sites in the  
516 partial octahedral sheets. If Fe can substitute only into limited sections of the allophane structure,  
517 this may also explain the previous finding of small Fe clusters in allophanes, even at very low



518 total Fe abundance (Baker and Strawn 2012; Baker et al. 2014). As noted above, Fe-Fe clustering  
519 is much less pronounced in the high-Si sample that was synthesized with Fe(II), although the  
520 XANES and EXAFS spectra indicate that the Fe in this sample was completely oxidized to  
521 Fe(III). However, modeling of the high-Al allophane sample synthesized with Fe(II), which still  
522 contained some residual Fe(II) upon XANES and EXAFS analysis, suggests that Fe clustering in  
523 this sample is comparable to that in samples synthesized with Fe(III). We hypothesize that this  
524 somewhat puzzling difference may have arisen from the different structures of the two  
525 endmember allophane types, with Fe clusters being more easily accommodated in the more  
526 extensive and fully-formed octahedral sheet of the high-Al allophane.

527         A previous XAFS study (Baker et al. 2014) examined natural and synthetic Fe-bearing  
528 imogolites and suggested that Fe in these samples was present at least partly in sorbed form,  
529 based on the resemblance of their XANES spectra to those of Fe-sorbed allophane samples.  
530 Examination of the XANES spectra of the samples in this study, particularly of the diagnostic  
531 pre-edge peaks, (Figure 9), suggests that coordination of Fe in the synthetic imogolite samples is  
532 similar to that of Fe in the allophane samples and that all Fe is in octahedral coordination.

### 533 **Compositional effects on allophane and imogolite spectra**

534         Terrestrial allophanic materials of different composition form in distinctively different  
535 environments (Parfitt 2009). Most imogolite and soil allophanes form by weathering of tephra,  
536 but allophane-like and imogolite-like materials have also been identified in soils with no obvious  
537 volcanic parent material, and variations in soil pH may lead to differences in the Al:Si ratio of  
538 allophanes (Yoshinaga and Aomine 1962a; Yoshinaga and Aomine 1962b; Tait et al. 1978;  
539 Farmer et al. 1980; Farmer and Fraser 1982; Parfitt and Kimble 1989). Unlike imogolite and  
540 proto-imogolite allophanes, naturally occurring high-Si stream-deposit allophanes from New

541 Zealand are deposited by thermal waters that have leached volcanic rocks and associated soils  
542 (Wells et al. 1977). If allophanes of different composition can be distinguished by remote  
543 sensing, this may aid in interpretation of how allophane deposits formed on Mars.

544 Changes in the mid-IR spectra of allophane due to differences in Si content are distinctive  
545 (Figures 2-4). Development of the strong band at  $1040\text{ cm}^{-1}$  arises from the polymerization of Si  
546 that is also reflected in the NMR spectra of these samples (Figure 8). This band development is  
547 apparent in emission spectra of the higher-Si 1:1 and 1:2 allophane samples (Figure 3),  
548 suggesting it should be detectable in remotely sensed data. If so, this will be significant in terms  
549 of using the presence of allophane to interpret formation conditions on Mars, since detection of  
550 high-Si allophanes would suggest formation around thermal features, whereas high-Al  
551 allophanes and imogolite would more likely have formed by weathering of tephra.

552 Several features of imogolite and allophane mid-IR reflectance spectra display detectable  
553 shifts to higher or lower wavelength with increasing Fe content (Figure 4). The Si-O stretching  
554 feature at  $1150\text{ cm}^{-1}$  in imogolite is shifted towards longer wavelengths with increasing Fe,  
555 although this shift is not observed for the allophanes in our study. Bands at  $495$  and  $415\text{ cm}^{-1}$   
556 shift to shorter wavelengths, and the Si-O-Al stretching vibration becomes a doublet at  $950$  and  
557  $1025\text{ cm}^{-1}$  in the high-Fe sample. The shifts observed in mid-IR reflectance spectra were not  
558 observed in thermal-IR emissivity spectra, suggesting they may not be detectable in TES data.

559 The Si-O-Al stretching band magnitude for allophanes increased with Fe(III) content in  
560 diffuse reflectance spectra (Figure 2). This darkening of the samples was less prominent in the  
561 1:1 allophane. A similar darkening was observed in VNIR reflectance spectra (Figure 4).  
562 Allophanes containing substituted Fe(II) displayed a similar but less intense increase in  
563 absorbance. At shorter wavelengths, increases in Fe content led to subtle broadening of the 1.9

564  $\mu\text{m}$   $\text{H}_2\text{O}$  combination band and 2.2  $\mu\text{m}$  OH combination band, probably due to the  
565 electronegativity of Fe(III) that is broadening the bond strengths.

566         The absence of observable Al-Fe-OH or Fe-Fe-OH bands suggests that detection of Fe in  
567 the allophane structure would be limited to higher concentrations than the highest in this study  
568 (Al:Fe 9:1). A previous spectroscopic study of Fe in smectites (Neumann et al. 2011) measured  
569 Al-Fe-OH bending at  $884\text{ cm}^{-1}$  in Wyoming montmorillonite, but only observed Fe-Al-OH and  
570 Fe-Fe-OH stretching bands in nontronites. Wyoming montmorillonite contains 2.5 total wt.% Fe  
571 with an octahedral Al:Fe ratio of  $\sim 7.3$  (Schoonheydt et al. 2011) and an ordered distribution of  
572 octahedral cations that would maximize the number of Al-Fe cation pairs present in the structure  
573 (Vantelon et al. 2003). Previous research has suggested that Fe substituted into allophanes forms  
574 small clusters in the octahedral sheet (Baker and Strawn 2012; Baker et al. 2014), which would  
575 effectively reduce the number of Fe-Al pairs from the ideal 9:1 suggested by the stoichiometry of  
576 the synthetic high-Fe allophane samples, and this may explain why Al-Fe-OH bands were not  
577 detected.

## 578 **Allophane structure**

579         The  $^{29}\text{Si}$  NMR data indicate significant differences between high-Al proto-imogolite  
580 allophane and high-Si allophane that are consistent with previous observations (Childs et al.  
581 1990; Childs et al. 1997; Childs et al. 1999; Parfitt 2009). These data suggest two different  
582 allophane structures that arise from variations in Al:Si ratio. Allophanes with high Al contents  
583 have an octahedral skeleton with individual orthosilicate tetrahedra attached to its interior. Some  
584 additional Si can be accommodated in the high-Al allophane structure through formation of  
585 polymerized Si chains. Allophanes with very high Si content are likely structured around a main  
586 tetrahedral Si and Al sheet skeleton, with additional Al in octahedral coordination. This could

587 resemble spheroidal halloysite (Joussein et al. 2005), or an aluminous analog of the “ferric  
588 kaolinite” structure that has been proposed for hisingerite nanospheres (Eggleton and Tilley  
589 1998; Baker and Strawn 2012), although the  $^{27}\text{Al}$  NMR peak position is more characteristic of  
590 2:1 dioctahedral phyllosilicates (Ildefonse et al. 1994). The high percentage of tetrahedral Al in  
591 the Al:Si 1:2 allophane (Table 1), however, indicates that the proportion of tetrahedral to  
592 octahedral cations in this sample is approximately 4:1. This very high proportion of cations in  
593 tetrahedral coordination indicates that only fragmental octahedral sheets are likely to be present.  
594 Deconvolved peaks at 1055 and 1176  $\text{cm}^{-1}$  in the infrared spectrum of the high-Si allophane  
595 (Figure 6) are similar to peak locations in opal, quartz, and feldspars, suggesting some Si in this  
596 sample may be accommodated in an opaline silica-like framework structure.

597         Previous work has suggested that allophanes whose bulk chemistry indicates an  
598 intermediate Al:Si ratio consist of a mixture of proto-imogolite allophane with a higher-Si form  
599 (Parfitt et al. 1980). However, the highest-Si naturally occurring allophanes are the “stream-  
600 deposit” allophanes, which occur in different environments than soil allophanes containing  
601 elevated Si. Therefore, it is unclear what composition represents the transition point between the  
602 two structures, or whether proto-imogolite and high-Si allophanes should even be considered as  
603 the same compound. It has been suggested that naturally occurring material previously identified  
604 as high-Al allophane is simply an imogolite precursor, even in samples where imogolite itself  
605 has not been identified, possibly due to kinetic limitations (Levard et al. 2012). Further  
606 experimental studies of higher-Si allophanes may help elucidate this structural question, and  
607 more detailed study of the range of natural allophanes identified as Si-rich, may help determine  
608 whether allophane-like materials containing polymerized Si should be treated as a phase distinct  
609 from proto-imogolite allophane.

610 Modelling of the Fe substituted allophanes aligns well with the previous results from  
611 Baker et al. (2014) in the Fe-O1, Fe-Fe, Fe-Al, and Fe-Si bond path lengths (Table 2). The Fe-O1  
612 shell at ~1.99 is consistent with Fe in octahedral coordination. Fe-Fe backscattering distances in  
613 the nanoball model show a negative correlation with the addition of Si into the structure, but this  
614 correlation is not present in the smectite modeled structure. Differences smaller than 0.02  
615 angstrom are typically unresolvable in EXAFS data (Ravel and Newville 2005). In all cases, Fe-  
616 Al backscattering paths were slightly shorter than Fe-Fe backscattering paths, likely due to the  
617 increased atomic radius of Fe as compared to Al.

618 One of the primary differences in the nanoball and smectite structures at this scale is the  
619 Fe-Si backscattering distance. In the nanoball structure, Fe-Si distances should be closer to 3.14.  
620 Modeled results show a range of distances from 3.23 to 3.28, much closer to the smectite  
621 structure of 3.18 to 3.24 modeled by Baker and Strawn (2014). An allophane model with  
622 polyhedral structure that had slightly curved faces rather than a sphere was proposed by Creton  
623 et al. (2008). If allophane has such a polyhedral structure, that may explain why the interatomic  
624 distances for the Fe-Si backscatterers observed in the present study are comparable to those in  
625 flat octahedral sheets rather than to modeled distances in a nanosphere.

## 626 **Remotely detecting Fe-allophane and Fe-imogolite on Mars**

627 Distinguishing between different X-ray amorphous materials on Mars using remotely  
628 sensed IR spectroscopy is difficult because the lack of long-range atomic order results in broader  
629 bands than are typical for their crystalline counterparts. Allophane and imogolite have been  
630 identified in specific regions on Mars through spectral modeling of TES data (Rampe et al.,  
631 2012) and in localized units using both TES models and band positions in CRISM spectra  
632 (Bishop and Rampe, 2016). Leached glass and allophane are spectrally similar in the thermal-IR

633 (e.g., Horgan and Bell, 2012), so the identification of regional allophane-bearing deposits on  
634 Mars via TES models is not unique. Considering TIR data cannot be used to distinguish between  
635 allophane and leached basaltic glass, it is unlikely that the small variations in allophane mid-IR  
636 reflectance spectra or imogolite TIR emissivity spectra from the incorporation of Fe into the  
637 structure would be observed in TES spectra. The Si/O ratio of X-ray amorphous materials can be  
638 distinguished using TES spectra (e.g., Michalski et al., 2005), so imogolite is spectrally distinct  
639 from 1:1 and 1:2 allophane, but it may be difficult to distinguish with certainty between  
640 amorphous aluminosilicates with similar Si/O ratios (e.g., imogolite and 2:1 allophane).

641         The detection of allophane vs. imogolite is more diagnostic in VNIR reflectance spectra  
642 from CRISM because of measurable differences in band positions (Bishop et al., 2013). Bishop  
643 and Rampe (2016) identified both allophane and imogolite in Mawrth Vallis based on the small  
644 differences in the bands at 1.92-1.93  $\mu\text{m}$  and 2.19-2.20  $\mu\text{m}$ . The incorporation of Fe into  
645 allophane and imogolite does not have a significant effect on these bands, so these bands cannot  
646 be used to determine whether the allophane and imogolite on Mars contain low levels of Fe.  
647 There are variations in the band intensities within the doublet at  $\sim 1.4 \mu\text{m}$  from the incorporation  
648 of Fe into the structure of allophane and imogolite, but the band near 1.4  $\mu\text{m}$  is often weak in  
649 CRISM spectra due to absorption from other components in the basaltic matrix, so this band also  
650 may not demonstrate whether allophane and imogolite on Mars contain Fe. VNIR bands  
651 resulting from Fe electronic transitions are present in multiple Fe-bearing minerals (e.g., Morris  
652 et al., 1985; Horgan et al., 2014; Bishop et al., 2015), so their presence in CRISM spectra from  
653 allophane- or imogolite-bearing terrains may not signify Fe is present in the allophane or  
654 imogolite structure, but their absence would indicate that the allophane or imogolite does not  
655 have Fe in its structure. A CRISM spectrum from an allophane- and imogolite-bearing unit in

656 Mawrth Vallis presented by Bishop and Rampe (2016; their Figure 1c) does not show a clear  
657 band at  $\sim 0.9 \mu\text{m}$ , suggesting that the allophane and imogolite in this unit likely do not contain Fe  
658 in their structures.

### 659 **Implications**

660 The structure of allophane varies with its composition, which in turn is a function of its  
661 formation conditions; the structure of imogolite resembles that of high-Al allophanes but is  
662 paracrystalline rather than poorly crystalline. Mid- and thermal-infrared spectra of allophanes are  
663 useful for distinguishing variations in Si content, and some spectral changes are also observed  
664 with varying Fe content in mid-IR reflectance spectra. Infrared spectra of imogolites are distinct  
665 from those of allophane, containing more and better-defined spectral bands. Increasing Fe  
666 substitution in imogolite produces recognizable broadening and shifts in some of these bands in  
667 the VNIR region. Thus, remotely sensed spectra of allophanic materials may contain information  
668 regarding the environment of formation and/or deposition of those materials. Although the  
669 occurrence of high-Al allophane and imogolite is generally considered to be indicative of early  
670 weathering of volcanic tephra, this is not universally true for terrestrial occurrences, and so these  
671 materials could potentially also represent weathering of a variety of parent materials under acidic  
672 conditions. Distinguishing between these possibilities will be important for characterizing  
673 allophane deposits on Mars, where tephra and acidic weathering conditions are both likely to  
674 have been important. Identification of high-Si allophane on Mars could potentially be indicative  
675 of deposition from thermal waters, and such a finding would be interpreted very differently in  
676 terms of the history of martian surface conditions.

677 Fe substitution into the allophane and imogolite structures cause small deviations in the  
678 spectra that may not be recognized from orbital data. This emphasizes the importance of





696  
697  
698  
699  
700  
701  
702  
703  
704  
705  
706  
707  
708  
709  
710  
711  
712  
713  
714  
715  
716  
717

## References

- Abidin, Z., Matsue, N. and Henmi, T. (2007) Differential formation of allophane and imogolite: experimental and molecular orbital study, *Journal of Computer-Aided Materials Design* 14, 1, 5-18.
- Abidin, Z., Matsue, N. and Henmi, T. (2008) A new method for nano tube imogolite synthesis, *Japanese Journal of Applied Physics* 47, 6S, 5079.
- Baker, L.L. and Strawn, D.G. (2012) Fe K-edge XAFS spectra of phyllosilicates of varying crystallinity, *Physics and Chemistry of Minerals* 39, 8, 675-684.
- Baker, L.L., Nickerson, R.D. and Strawn, D.G. (2014) XAFS study of Fe-substituted allophane and imogolite, *Clays and Clay Minerals* 62, 1, 20-34.
- Bandfield, J.L., Hamilton, V.E. and Christensen, P.R. (2000) A global view of Martian surface compositions from MGS-TES, *Science* 287, 5458, 1626-1630.
- Bell, J.F., McCord, T.B. and Owensby, P.D. (1990) Observational evidence of crystalline iron oxides on Mars, *Journal of Geophysical Research: Solid Earth* 95, B9, 14447-14461.
- Bishop, J.L. and Rampe, E.B. (2016) Evidence for a changing Martian climate from the mineralogy at Mawrth Vallis, *Earth and Planetary Science Letters* 448, 42-48.
- Bishop, J.L., Rampe, E.B., Bish, D.L., Abidin, Z., Baker, L.L., Matsue, N. and Henmi, T. (2013) Spectral and hydration properties of allophane and imogolite, *Clays and Clay Minerals* 61, 1, 57-74.
- Bishop, J.L., Fairén, A.G., Michalski, J.R., Gago-Duport, L., Baker, L.L., Velbel, M.A., Gross, C. and Rampe, E.B. (2018) Surface clay formation during short-term warmer and wetter conditions on a largely cold ancient Mars, *Nature Astronomy* 2, 206-213.

- 718 Bishop, J.L., Dobrea, E.Z.N., McKeown, N.K., Mario Parente, Ehlmann, B.L., Michalski, J.R.,  
719 Milliken, R.E., Poulet, F., Swayze, G.A., Mustard, J.F., Murchie, S.L. and Bibring, J.-P.  
720 (2008) Phyllosilicate diversity and past aqueous activity revealed at Mawrth Vallis, Mars,  
721 Science 321, 830-833.
- 722 Blake, D.F., Morris, R., Kocurek, G., Morrison, S., Downs, R., Bish, D., Ming, D., Edgett, K.,  
723 Rubin, D. and Goetz, W. (2013) Curiosity at Gale crater, Mars: Characterization and  
724 analysis of the Rocknest sand shadow, Science 341, 6153, 1239505.
- 725 Bristow, T.F., Rampe, E.B., Achilles, C.N., Blake, D.F., Chipera, S.J., Craig, P., Crisp, J.A., Des  
726 Marais, D.J., Downs, R.T., Gellert, R., Grotzinger, J.P., Gupta, S., Hazen, R.M., Horgan,  
727 B., Hogancamp, J.V., Mangold, N., Mahaffy, P.R., McAdam, A.C., Ming, D.W.,  
728 Morookian, J.M., Morris, R.V., Morrison, S.M., Treiman, A.H., Vaniman, D.T.,  
729 Vasavada, A.R. and Yen, A.S. (2018) Clay mineral diversity and abundance in  
730 sedimentary rocks of Gale crater, Mars, Science Advances 4, 6, eaar3330.
- 731 Childs, C., Inoue, K., Seyama, H., Soma, M., Theng, B. and Yuan, G. (1997) X-ray  
732 photoelectron spectroscopic characterization of Silica Springs allophane, Clay Minerals  
733 32, 4, 565-572.
- 734 Childs, C.W., Parfitt, R.L. and Newman, R.H. (1990) Structural studies of Silica Springs  
735 allophane, Clay Minerals 25, 3, 329-341.
- 736 Childs, C.W., Hayashi, S. and Newman, R.H. (1999) Five-coordinate aluminum in allophane,  
737 Clays and Clay Minerals 47, 1, 64-69.
- 738 Christensen, P.R. and Harrison, S.T. (1993) Thermal infrared emission spectroscopy of natural  
739 surfaces: Application to desert varnish coatings on rocks, Journal of Geophysical  
740 Research: Solid Earth 98, B11, 19819-19834.

- 741 Christensen, P.R., Bandfield, J.L., Hamilton, V.E., Ruff, S.W., Kieffer, H.H., Titus, T.N., Malin,  
742 M.C., Morris, R.V., Lane, M.D. and Clark, R. (2001) Mars Global Surveyor Thermal  
743 Emission Spectrometer experiment: investigation description and surface science results,  
744 Journal of Geophysical Research: Planets 106, E10, 23823-23871.
- 745 Cradwick, P.D.G., Farmer, V.C., Russell, J.D., Masson, C.R., Wada, K. and Yoshinaga, N.  
746 (1972) Imogolite, a hydrated aluminum silicate of tubular structure, Nature Physical  
747 Science 240, 187-189.
- 748 Creton, B., Bougeard, D., Smirnov, K.S., Guilment, J. and Poncelet, O.G. (2008a) Structural  
749 model and computer modeling study of allophane, Journal of Physical Chemistry C 112,  
750 2, 358-364.
- 751 Creton, B., Bougeard, D., Smirnov, K.S., Guilment, J. and Poncelet, O. (2008b) Molecular  
752 dynamics study of hydrated imogolite. 1. Vibrational dynamics of the nanotube, The  
753 Journal of Physical Chemistry C 112, 27, 10013-10020.
- 754 Eggleton, R.A. and Tilley, D.B. (1998) Hisingerite; a ferric kaolin mineral with curved  
755 morphology, Clays and Clay Minerals 46, 4, 400-413.
- 756 Ehlmann, B.L., Mustard, J.F., Swayze, G.A., Clark, R.N., Bishop, J.L., Poulet, F., Des Marais,  
757 D.J., Roach, L.H., Milliken, R.E., Wray, J.J., Barnouin-Jha, O. and Murchie, S.L. (2009)  
758 Identification of hydrated silicate minerals on Mars using MRO-CRISM: Geologic  
759 context near Nili Fossae and implications for aqueous alteration, J. Geophys. Res. 114,  
760 E00D08.
- 761 Farmer, V. (1997) Conversion of ferruginous allophanes to ferruginous beidellites at 95° under  
762 alkaline conditions with alternating oxidation and reduction, Clays and Clay Minerals 45,  
763 4, 591-597.

- 764 Farmer, V., Krishnamurti, G. and Huang, P. (1991) Synthetic allophane and layer-silicate  
765 formation in  $\text{SiO}_2\text{-Al}_2\text{O}_3\text{-FeO-Fe}_2\text{O}_3\text{-MgO-H}_2\text{O}$  systems at 23 C and 89 C in a  
766 calcareous environment, *Clays and Clay Minerals* 39, 561-570.
- 767 Farmer, V.C. and Fraser, A.R. (1982) Chemical and colloidal stability of sols in the  $\text{Al}_2\text{O}_3\text{-}$   
768  $\text{Fe}_2\text{O}_3\text{-SiO}_2\text{-H}_2\text{O}$  system: their role in podzolization, *Journal of Soil Science* 33, 4, 737-  
769 742.
- 770 Farmer, V.C., Russell, J.D. and Berrow, M.L. (1980) Imogolite and proto-imogolite allophane in  
771 spodic horizons: Evidence for a mobile aluminium silicate in podzol formation *Journal of*  
772 *Soil Science* 31, 4, 673-684.
- 773 Guimarães, L., Enyashin, A.N., Frenzel, J., Heine, T., Duarte, H.A. and Seifert, G. (2007)  
774 Imogolite nanotubes: stability, electronic, and mechanical properties, *ACS Nano* 1, 4,  
775 362-368.
- 776 Henmi, T. and Wada, K. (1976) Morphology and composition of allophane, *American*  
777 *Mineralogist* 61, 5-6, 379-390.
- 778 Horgan, B. and Bell, J.F. (2012) Widespread weathered glass on the surface of Mars, *Geology*  
779 40, 5, 391-394.
- 780 Horikawa, Y. and Soezima, H. (1977) State analysis of iron in allophanic clays II: Iron L-  
781 emission band spectra from allophanic clays and hisingerite by the use of an X-ray  
782 microanalyzer, *Clay Science* 5, 2, 97-102.
- 783 Ildefonse, P., Kirkpatrick, R.J., Montez, B., Calas, G., Flank, A.M. and Lagarde, P. (1994) 27 Al  
784 MAS NMR and aluminum X-ray absorption near edge structure study of imogolite and  
785 allophanes, *Clays and Clay Minerals* 42, 3, 276-287.

- 786 Joussein, E., Petit, S., Churchman, J., Theng, B., Righi, D. and Delvaux, B. (2005) Halloysite  
787 clay minerals -- a review, *Clay Minerals* 40, 4, 383-426.
- 788 Kitagawa, Y. (1973) Substitution of aluminum by iron in allophane, *Clay Science* 4, 4, 151-154.
- 789 Klingelhöfer, G., Morris, R.V., Bernhardt, B., Schröder, C., Rodionov, D.S., de Souza, P.A.,  
790 Yen, A., Gellert, R., Evlanov, E.N., Zubkov, B., Foh, J., Bonnes, U., Kankeleit, E.,  
791 Gütlich, P., Ming, D.W., Renz, F., Wdowiak, T., Squyres, S.W. and Arvidson, R.E.  
792 (2004) Jarosite and Hematite at Meridiani Planum from Opportunity's Mössbauer  
793 Spectrometer, *Science* 306, 5702, 1740.
- 794 Levard, C., Doelsch, E., Basile-Doelsch, I., Abidin, Z., Mische, H., Masion, A., Rose, J.,  
795 Borschneck, D. and Bottero, J.Y. (2012) Structure and distribution of allophanes,  
796 imogolite and proto-imogolite in volcanic soils, *Geoderma* 183–184, 100-108.
- 797 Levard, C., Rose, J., Thill, A., Masion, A., Doelsch, E., Maillet, P., Spalla, O., Olivi, L.,  
798 Cognigni, A., Ziarelli, F. and Bottero, J.Y. (2010) Formation and growth mechanisms of  
799 imogolite-like aluminogermanate nanotubes, *Chemistry of Materials* 22, 8, 2466-2473.
- 800 Loewenstein, W. (1954) The distribution of aluminum in the tetrahedra of silicates and  
801 aluminates, *American Mineralogist: Journal of Earth and Planetary Materials* 39, 1-2, 92-  
802 96.
- 803 MacKenzie, K.J.D., Bowden, M.E. and Meinhold, R.H. (1991) The structure and thermal  
804 transformations of allophanes studied by  $^{29}\text{Si}$  and  $^{27}\text{Al}$  high resolution solid-state  
805 NMR, *Clays and Clay Minerals* 39, 4, 337-346.
- 806 McBride, M.B., Farmer, V.C., Russell, J.D., Tait, J.M. and Goodman, B.A. (1984) Iron  
807 substitution in aluminosilicate sols synthesized at low pH, *Clay Minerals* 19, 1, 1-8.

- 808 Michalski, J.R., Kraft, M.D., Sharp, T.G. and Christensen, P.R. (2006) Effects of chemical  
809 weathering on infrared spectra of Columbia River Basalt and spectral interpretations of  
810 martian alteration, *Earth and Planetary Science Letters* 248, 3, 822-829.
- 811 Michalski, J.R., Kraft, M.D., Sharp, T.G., Williams, L.B. and Christensen, P.R. (2005)  
812 Mineralogical constraints on the high-silica martian surface component observed by TES,  
813 *Icarus* 174, 1, 161-177.
- 814 Milliken, R.E., Swayze, G.A., Arvidson, R.E., Bishop, J.L., Clark, R.N., Ehlmann, B.L., Green,  
815 R.O., Grotzinger, J.P., Morris, R.V., Murchie, S.L., Mustard, J.F. and Weitz, C. (2008)  
816 Opaline silica in young deposits on Mars, *Geology* 36, 11, 847-850.
- 817 Ming, D.W., Archer, P.D., Glavin, D.P., Eigenbrode, J.L., Franz, H.B., Sutter, B., Brunner, A.E.,  
818 Stern, J.C., Freissinet, C., McAdam, A.C., Mahaffy, P.R., Cabane, M., Coll, P.,  
819 Campbell, J.L., Atreya, S.K., Niles, P.B., Bell, J.F., Bish, D.L., Brinckerhoff, W.B.,  
820 Buch, A., Conrad, P.G., Des Marais, D.J., Ehlmann, B.L., Fairén, A.G., Farley, K.,  
821 Flesch, G.J., Francois, P., Gellert, R., Grant, J.A., Grotzinger, J.P., Gupta, S., Herkenhoff,  
822 K.E., Hurowitz, J.A., Leshin, L.A., Lewis, K.W., McLennan, S.M., Miller, K.E.,  
823 Moersch, J., Morris, R.V., Navarro-González, R., Pavlov, A.A., Perrett, G.M., Pradler, I.,  
824 Squyres, S.W., Summons, R.E., Steele, A., Stolper, E.M., Sumner, D.Y., Szopa, C.,  
825 Teinturier, S., Trainer, M.G., Treiman, A.H., Vaniman, D.T., Vasavada, A.R., Webster,  
826 C.R., Wray, J.J. and Yingst, R.A. (2014) Volatile and Organic Compositions of  
827 Sedimentary Rocks in Yellowknife Bay, Gale Crater, Mars, *Science* 343, 6169, 1245267.
- 828 Montarges-Pelletier, E., Bogenez, S., Pelletier, M., Razafitianamaharavo, A., Ghanbaja, J.,  
829 Lartiges, B. and Michot, L. (2005) Synthetic allophane-like particles: textural properties,  
830 *Colloids and Surfaces A: Physicochemical and Engineering Aspects* 255, 1-3, 1-10.

- 831 Morris, R.V. and Lauer, H.V. (1990) Matrix effects for reflectivity spectra of dispersed  
832 nanophase (superparamagnetic) hematite with application to Martian spectral data,  
833 Journal of Geophysical Research: Solid Earth 95, B4, 5101-5109.
- 834 Morris, R.V., Klingelhöfer, G., Bernhardt, B., Schröder, C., Rodionov, D.S., de Souza, P.A.,  
835 Yen, A., Gellert, R., Evlanov, E.N., Foh, J., Kankeleit, E., Gütlich, P., Ming, D.W., Renz,  
836 F., Wdowiak, T., Squyres, S.W. and Arvidson, R.E. (2004) Mineralogy at Gusev Crater  
837 from the Mössbauer Spectrometer on the Spirit Rover, Science 305, 5685, 833.
- 838 Morris, R.V., Klingelhöfer, G., Schröder, C., Rodionov, D.S., Yen, A., Ming, D.W., de Souza  
839 Jr., P.A., Fleischer, I., Wdowiak, T., Gellert, R., Bernhardt, B., Evlanov, E.N., Zubkov,  
840 B., Foh, J., Bonnes, U., Kankeleit, E., Gütlich, P., Renz, F., Squyres, S.W. and Arvidson,  
841 R.E. (2006a) Mössbauer mineralogy of rock, soil, and dust at Gusev crater, Mars: Spirit's  
842 journey through weakly altered olivine basalt on the plains and pervasively altered basalt  
843 in the Columbia Hills, Journal of Geophysical Research: Planets 111, E2.
- 844 Morris, R.V., Klingelhöfer, G., Schröder, C., Rodionov, D.S., Yen, A., Ming, D.W., de Souza,  
845 P.A., Wdowiak, T., Fleischer, I., Gellert, R., Bernhardt, B., Bonnes, U., Cohen, B.A.,  
846 Evlanov, E.N., Foh, J., Gütlich, P., Kankeleit, E., McCoy, T., Mittlefehldt, D.W., Renz,  
847 F., Schmidt, M.E., Zubkov, B., Squyres, S.W. and Arvidson, R.E. (2006b) Mössbauer  
848 mineralogy of rock, soil, and dust at Meridiani Planum, Mars: Opportunity's journey  
849 across sulfate-rich outcrop, basaltic sand and dust, and hematite lag deposits, Journal of  
850 Geophysical Research: Planets 111, E12, n/a-n/a.
- 851 Morrison, S.M., Downs, R.T., Blake, D.F., Vaniman, D.T., Ming, D.W., Hazen, R.M., Treiman,  
852 A.H., Achilles, C.N., Yen, A.S., Morris, R.V., Rampe, E.B., Bristow, T.F., Chipera, S.J.,  
853 Sarrazin, P.C., Gellert, R., Fendrich, K.V., Morookian, J.M., Farmer, J.D., Des Marais,

- 854 D.J. and Craig, P.I. (2018) Crystal chemistry of martian minerals from Bradbury Landing  
855 through Naukluft Plateau, Gale crater, Mars, American Mineralogist 103, 6, 857-871.
- 856 Murchie, S.L., Mustard, J.F., Ehlmann, B.L., Milliken, R.E., Bishop, J.L., McKeown, N.K., Noe  
857 Dobrea, E.Z., Seelos, F.P., Buczkowski, D.L., Wiseman, S.M., Arvidson, R.E., Wray,  
858 J.J., Swayze, G., Clark, R.N., Des Marais, D.J., McEwen, A.S. and Bibring, J.-P. (2009)  
859 A synthesis of Martian aqueous mineralogy after 1 Mars year of observations from the  
860 Mars Reconnaissance Orbiter, Journal of Geophysical Research-Planets 114, E00D06.
- 861 Neumann, A., Petit, S. and Hofstetter, T.B. (2011) Evaluation of redox-active iron sites in  
862 smectites using middle and near infrared spectroscopy, Geochimica et Cosmochimica  
863 Acta 75, 9, 2336-2355.
- 864 Parfitt, R. (1990) Allophane in New Zealand-a review, Soil Research 28, 3, 343-360.
- 865 Parfitt, R.L. (2009) Allophane and imogolite: role in soil biogeochemical processes, Clay  
866 Minerals 44, 1, 135-155.
- 867 Parfitt, R.L. and Kimble, J.M. (1989) Conditions for Formation of Allophane in Soils, Soil  
868 Science Society of America Journal 53, 3, 971-977.
- 869 Parfitt, R.L., Furkert, R.J. and Henmi, T. (1980) Identification and structure of two types of  
870 allophane from volcanic ash soils and tephra, Clays and Clay Minerals 28, 5, 328-334.
- 871 Rajan, S.S.S. (1979) Adsorption and Desorption of Sulfate and Charge Relationships in  
872 Allophanic Clays<sup>1</sup>, Soil Science Society of America Journal 43, 1, 65-69.
- 873 Rampe, E., Kraft, M., Sharp, T., Golden, D., Ming, D. and Christensen, P. (2012) Allophane  
874 detection on Mars with Thermal Emission Spectrometer data and implications for  
875 regional-scale chemical weathering processes, Geology 40, 11, 995-998.



- 876 Rampe, E.B., Morris, R., V., Archer, P.D., Agresti, D.G. and Ming, D.W. (2016) Recognizing  
877 sulfate and phosphate complexes chemisorbed onto nanophase weathering products on  
878 Mars using in-situ and remote observations. American Mineralogist. 101: 678 p.
- 879 Ravel, B. (2001) ATOMS: crystallography for the X-ray absorption spectroscopist, Journal of  
880 Synchrotron Radiation 8, 314-316.
- 881 Ravel, B. and Newville, M. (2005) ATHENA, ARTEMIS, HEPHAESTUS: data analysis for X-  
882 ray absorption spectroscopy using IFEFFIT, Journal of Synchrotron Radiation 12, 4, 537-  
883 541.
- 884 Rice, M.S., Bell, J.F., Cloutis, E.A., Wang, A., Ruff, S.W., Craig, M.A., Bailey, D.T., Johnson,  
885 J.R., de Souza, P.A. and Farrand, W.H. (2010) Silica-rich deposits and hydrated minerals  
886 at Gusev Crater, Mars: Vis-NIR spectral characterization and regional mapping, Icarus  
887 205, 2, 375-395.
- 888 Rogers, A.D. and Christensen, P.R. (2007) Surface mineralogy of Martian low-albedo regions  
889 from MGS-TES data: Implications for upper crustal evolution and surface alteration,  
890 Journal of Geophysical Research: Planets 112, E1.
- 891 Ruff, S.W. and Christensen, P. (2007) Basaltic andesite, altered basalt, and a TES-based search  
892 for smectite clay minerals on Mars, Geophysical research letters 34, 10.
- 893 Ruff, S.W., Christensen, P.R., Barbera, P.W. and Anderson, D.L. (1997) Quantitative thermal  
894 emission spectroscopy of minerals: A laboratory technique for measurement and  
895 calibration, Journal of Geophysical Research: Solid Earth 102, B7, 14899-14913.
- 896 Ruff, S.W., Farmer, J.D., Calvin, W.M., Herkenhoff, K.E., Johnson, J.R., Morris, R.V., Rice,  
897 M.S., Arvidson, R.E., Bell III, J.F., Christensen, P.R. and Squyres, S.W. (2011)

- 898 Characteristics, distribution, origin, and significance of opaline silica observed by the  
899 Spirit rover in Gusev crater, Mars, *Journal of Geophysical Research: Planets* 116, E7.
- 900 Schoonheydt, R.A., Johnston, C.T., Brigatti, M.F. and Mottana, A. (2011) The surface properties  
901 of clay minerals, In *Layered Mineral Structures and their Application in Advanced*  
902 *Technologies* Ed., pp. 0, Mineralogical Society of Great Britain and Ireland.
- 903 Singer, R.B. (1982) Spectral evidence for the mineralogy of high-albedo soils and dust on Mars,  
904 *Journal of Geophysical Research: Solid Earth* 87, B12, 10159-10168.
- 905 Skok, J.R., Mustard, J.F., Ehlmann, B.L., Milliken, R.E. and Murchie, S.L. (2010) Silica deposits  
906 in the Nili Patera caldera on the Syrtis Major volcanic complex on Mars, *Nature*  
907 *Geoscience* 3, 838.
- 908 Squyres, S.W., Arvidson, R.E., Ruff, S., Gellert, R., Morris, R.V., Ming, D.W., Crumpler, L.,  
909 Farmer, J.D., Marais, D.J.D., Yen, A., McLennan, S.M., Calvin, W., Bell, J.F., Clark,  
910 B.C., Wang, A., McCoy, T.J., Schmidt, M.E. and de Souza, P.A. (2008) Detection of  
911 Silica-Rich Deposits on Mars, *Science* 320, 5879, 1063.
- 912 Tait, J., Yoshinaga, N. and Mitchell, B. (1978) The occurrence of imogolite in some Scottish  
913 soils, *Soil Science and Plant Nutrition* 24, 1, 145-151.
- 914 Thill, A. (2016) Characterisation of imogolite by microscopic and spectroscopic methods, In  
915 *Developments in Clay Science*. Yuan, P., Thill, A. and Bergaya, F., Ed., pp. 223-253,  
916 Elsevier.
- 917 Tsipursky, S.I. and Drits, V.A. (1984) The distribution of octahedral cations in the 2:1 layers of  
918 dioctahedral smectites studied by oblique-texture electron diffraction, *Clay Minerals* 19,  
919 2, 177-193.

- 920 Vaniman, D.T., Bish, D.L., Ming, D.W., Bristow, T.F., Morris, R.V., Blake, D.F., Chipera, S.J.,  
921 Morrison, S.M., Treiman, A.H., Rampe, E.B., Rice, M., Achilles, C.N., Grotzinger, J.P.,  
922 McLennan, S.M., Williams, J., Bell, J.F., Newsom, H.E., Downs, R.T., Maurice, S.,  
923 Sarrazin, P., Yen, A.S., Morookian, J.M., Farmer, J.D., Stack, K., Milliken, R.E.,  
924 Ehlmann, B.L., Sumner, D.Y., Berger, G., Crisp, J.A., Hurowitz, J.A., Anderson, R., Des  
925 Marais, D.J., Stolper, E.M., Edgett, K.S., Gupta, S. and Spanovich, N. (2014) Mineralogy  
926 of a Mudstone at Yellowknife Bay, Gale Crater, Mars, *Science* 343, 6169, 1243480.
- 927 Vantelon, D., Montarges-Pelletier, E., Michot, L.J., Pelletier, M., Thomas, F. and Briois, V.  
928 (2003) Iron distribution in the octahedral sheet of dioctahedral smectites. An Fe K-edge  
929 X-ray absorption spectroscopy study, *Physics and Chemistry of Minerals* 30, 1, 44-53.
- 930 Weitz, C.M., Bishop, J.L., Baker, L.L. and Berman, D.C. (2014) Fresh exposures of hydrous Fe-  
931 bearing amorphous silicates on Mars, *Geophysical Research Letters* 41, 24, 8744-8751.
- 932 Wells, N., Childs, C. and Downes, C. (1977) Silica Springs, Tongariro National Park, New  
933 Zealand—analyses of the spring water and characterisation of the alumino-silicate  
934 deposit, *Geochimica et cosmochimica acta* 41, 10, 1497-1506.
- 935 Wyatt, M.B. and McSween Jr, H.Y. (2002) Spectral evidence for weathered basalt as an  
936 alternative to andesite in the northern lowlands of Mars, *Nature* 417, 263.
- 937 Yoshinaga, N. and Aomine, S. (1962a) Imogolite in some Ando soils, *Soil Science and Plant*  
938 *Nutrition* 8, 3, 22-29.
- 939 Yoshinaga, N. and Aomine, S. (1962b) Allophane in Some Ando Soils, *Soil Science and Plant*  
940 *Nutrition* 8, 2, 6-13.

941

942



944 **Figure Captions**

945 Figure 1: Schematic cross-section of a high-Al allophane nanoball with Fe present in octahedral  
946 substitution for an Al atom.

947 Figure 2: Kubelka-Munk transformed diffuse reflectance mid-IR spectra for synthetic allophanes  
948 and imogolite of varying Fe content mixed with KBr. Vertical solid and dashed lines at 950,  
949 1050, 3400, and 3500  $\text{cm}^{-1}$  indicate the respective locations of characteristic OH-stretching and  
950 Si-O-Al bending features in imogolite and high-Si allophane as discussed in the text.

951 Figure 3: Thermal-IR emissivity spectra for Fe-free and Fe-bearing synthetic allophanes and  
952 imogolite. Solid and dashed lines at 1045, 950, 935, 590, 556, 538, 495, and 484  $\text{cm}^{-1}$  indicate  
953 the locations of characteristic spectral features discussed in the text.

954 Figure 4: a. Mid-IR reflectance spectra for selected synthetic allophanes and imogolite. Solid and  
955 dashed vertical lines indicate the locations of characteristic spectral features, and arrows indicate  
956 the direction of band shifts with increasing Fe content, as discussed in the text. b. Expanded  
957 section of Figure 4a from the gray box.

958 Figure 5: a. VNIR reflectance spectra of selected synthetic allophanes and imogolites with  
959 varying Fe abundances. Dashed lines indicate electronic transition bands that develop as Fe  
960 content increases; dotted and solid lines indicate band centers that shift as Fe content changes. b.  
961 Expanded section of Figure 5a from the grey box. Spectra are offset for clarity.

962 Figure 6: Peak fitting of Fe-free, high Si allophane sample showing deconvolved peaks at 893,  
963 1055, and 1175  $\text{cm}^{-1}$ .

964 Figure 7.  $^{27}\text{Al}$  Magic angle spinning nuclear magnetic resonance spectra for Fe-free allophanes  
965 and imogolite. Spectra have been vertically offset for clarity.

966 Figure 8.  $^{29}\text{Si}$  Magic angle spinning nuclear magnetic resonance spectra for Fe-free allophanes  
967 and imogolite. Spectra have been vertically offset for clarity.

968 Figure 9: a. XANES spectra and b. first derivative spectra of Fe-bearing allophanes and  
969 imogolite. Spectra have been vertically offset for clarity. Arrows indicate location of feature  
970 discussed in the text.

971 Figure 10: a. EXAFS chi spectra and b. Fourier transformed spectra of Fe-bearing allophanes and  
972 imogolite. Spectra have been vertically offset for clarity. Dashed curves show fits to Fe-bearing  
973 allophane spectra using the montmorillonite 5-shell model.

974 Table 1. Synthesized allophane nominal and measured compositions. A pseudo-cationic formula is given for each sample assuming  
 975 sufficient O to coordinate the Al, Fe, and Si present. The presence of hydroxyl is indicated but total water in the samples was not  
 976 determined.

977

Sample	Nominal compositions (mol ratios)			Actual compositions (mol ratios)			Al coordination (%)			Formula
	(Al+Fe):Si	Fe(III):Al	Fe(II):Al	Al:Si	Fe:Al	(Al+Fe):Si	Al <sub>T</sub>	Al <sub>P</sub>	Al <sub>O</sub>	
100516-2:1	2	0	0	2.02	0	2.02	6.2	3.1	90.5	Al <sub>2</sub> O <sub>3</sub> SiO <sub>2</sub> (OH) <sub>n</sub>
121916-2:1	2	0.02	0	1.97	0.0204	2.01	-	-	-	Al <sub>1.97</sub> Fe <sub>0.04</sub> O <sub>3</sub> SiO <sub>2</sub> (OH) <sub>n</sub>
011917-2:1	2	0.05	0	1.91	0.0526	2.02	-	-	-	Al <sub>1.91</sub> Fe <sub>0.1</sub> O <sub>3</sub> SiO <sub>2</sub> (OH) <sub>n</sub>
013117-2:1	2	0.1	0	1.82	0.111	2.02	-	-	-	Al <sub>1.82</sub> Fe <sub>0.22</sub> O <sub>3</sub> SiO <sub>2</sub> (OH) <sub>n</sub>
030917-2:1	2	0	0.1	1.81	0.111	2.02	-	-	-	Al <sub>1.81</sub> Fe <sub>0.22</sub> O <sub>3</sub> SiO <sub>2</sub> (OH) <sub>n</sub>
101716-1:1	1	0	0	1.02	0	1.02	27.9	3.6	68.5	Al <sub>2</sub> O <sub>3</sub> (SiO <sub>2</sub> ) <sub>2</sub> (OH) <sub>n</sub>
103116-1:1	1	0.02	0	1.02	0.0203	1.05	-	-	-	Al <sub>2.04</sub> Fe <sub>0.04</sub> O <sub>3</sub> (SiO <sub>2</sub> ) <sub>2</sub> (OH) <sub>n</sub>
110716-1:1	1	0.05	0	1.01	0.0524	1.06	-	-	-	Al <sub>2.02</sub> Fe <sub>0.1</sub> O <sub>3</sub> (SiO <sub>2</sub> ) <sub>2</sub> (OH) <sub>n</sub>
111416-1:1	1	0.1	0	0.95	0.111	1.05	-	-	-	Al <sub>1.9</sub> Fe <sub>0.22</sub> O <sub>3</sub> (SiO <sub>2</sub> ) <sub>2</sub> (OH) <sub>n</sub>
102416-1:2	0.5	0	0	0.50	0	0.50	42.3	n.d.	57.7	Al <sub>2</sub> O <sub>3</sub> (SiO <sub>2</sub> ) <sub>4</sub> (OH) <sub>n</sub>
121116-1:2	0.5	0.02	0	0.52	0.0204	0.53	-	-	-	Al <sub>2.08</sub> Fe <sub>0.04</sub> O <sub>3</sub> (SiO <sub>2</sub> ) <sub>4</sub> (OH) <sub>n</sub>
112816-1:2	0.5	0.05	0	0.50	0.0526	0.53	-	-	-	Al <sub>2.0</sub> Fe <sub>0.21</sub> O <sub>3</sub> (SiO <sub>2</sub> ) <sub>4</sub> (OH) <sub>n</sub>
120416-1:2	0.5	0.1	0	0.48	0.111	0.53	-	-	-	Al <sub>1.92</sub> Fe <sub>0.44</sub> O <sub>3</sub> (SiO <sub>2</sub> ) <sub>4</sub> (OH) <sub>n</sub>
040117-1:2	0.5	0	0.1	-	-	-	-	-	-	-

978 - not analyzed  
 979 n.d. not detected

980

981

982

983 Table 2. Fitting results for allophane samples. CN: coordination number. R: interatomic distance (Å).  $\sigma^2$ : Debye-Waller factor (Å<sup>2</sup>).

Nanoball Model															
120416-1:2 Al:Si 1:2 10% Fe(III)				111416-1:1 Al:Si 1:1 10% Fe(III)			013117-2:1 Al:Si 2:1 10% Fe(III)			040117-1:2 Al:Si 1:2 10% Fe(II)*			030917-2:1 Al:Si 2:1 10% Fe(II)**		
Path	E0		-3.043	E0		-3.787	E0		-4.111	E0		-1.554	E0		-4.776
	R factor		0.004	R factor		0.011	R factor		0.007	R factor		0.011	R factor		0.011
	CN	R	$\sigma^2$	CN	R	$\sigma^2$	CN	R	$\sigma^2$	CN	R	$\sigma^2$	CN	R	$\sigma^2$
Fe-O1	6	1.99	0.006	6	1.99	0.006	6	1.97	0.008	6	1.99	0.009	6	1.99	0.007
Fe-Fe	1.96	3.06	0.006	1.63	3.03	0.006	1.67	3.00	0.008	1.50	3.06	0.009	0.58	3.01	0.007
Fe-Al	1.04	3.04	0.006	1.37	3.01	0.006	1.33	2.99	0.008	1.50	3.01	0.009	2.42	3.02	0.007
Fe-Si	3	3.28	0.006	3	3.28	0.006	3	3.24	0.008	3	3.26	0.009	3	3.27	0.007
Fe-O2	6	3.79	0.030	6	3.76	0.023	6	3.75	0.022	6	3.68	0.040	6	3.72	0.019
Fe-O3	3	3.98	0.030	3	3.98	0.023	3	3.98	0.022	3	3.98	0.040	3	3.98	0.019
Smectite Model															
120416-1:2 Al:Si 1:2 10% Fe(III)				111416-1:1 Al:Si 1:1 10% Fe(III)			013117-2:1 Al:Si 2:1 10% Fe(III)			040117-1:2 Al:Si 1:2 10% Fe(II)*			030917-2:1 Al:Si 2:1 10% Fe(II)**		
Path	E0		-2.325	E0		-2.498	E0		-3.255	E0		0.364	E0		-3.968
	R factor		0.005	R factor		0.006	R factor		0.008	R factor		0.012	R factor		0.011
	CN	R	$\sigma^2$	CN	R	$\sigma^2$	CN	R	$\sigma^2$	CN	R	$\sigma^2$	CN	R	$\sigma^2$
Fe-O1	6	1.99	0.006	6	1.99	0.006	6	1.97	0.008	6	2.00	0.010	6	1.99	0.007
Fe-Fe	2.01	3.05	0.006	2.22	3.06	0.006	2.10	3.03	0.008	2.22	3.08	0.010	0.95	3.03	0.007
Fe-Al	0.99	3.01	0.006	0.78	3.06	0.006	0.90	3.04	0.008	0.78	3.02	0.010	2.05	3.02	0.007
Fe-Si	2	3.28	0.006	2	3.26	0.006	2	3.23	0.008	2	3.23	0.010	2	3.28	0.007
Fe-O2	1	3.51	0.052	1	3.50	0.018	1	3.34	0.029	1	3.38	0.028	1	3.39	0.029
Fe-O3	6	3.70	0.052	6	3.79	0.018	6	3.70	0.029	6	3.70	0.028	6	3.70	0.029

984 \*Although this sample was synthesized using Fe(II), XAFS results indicated that most or all Fe in it was oxidized to Fe(III) prior to analysis, as  
 985 discussed in the text.

986 \*\* This sample was synthesized using Fe(II); XAFS results indicated that some Fe in it was oxidized to Fe(III) prior to analysis, as discussed in  
 987 the text.



# FIG 1

## Cross Section of Fe-Substituted Proto-Imogolite Allophane

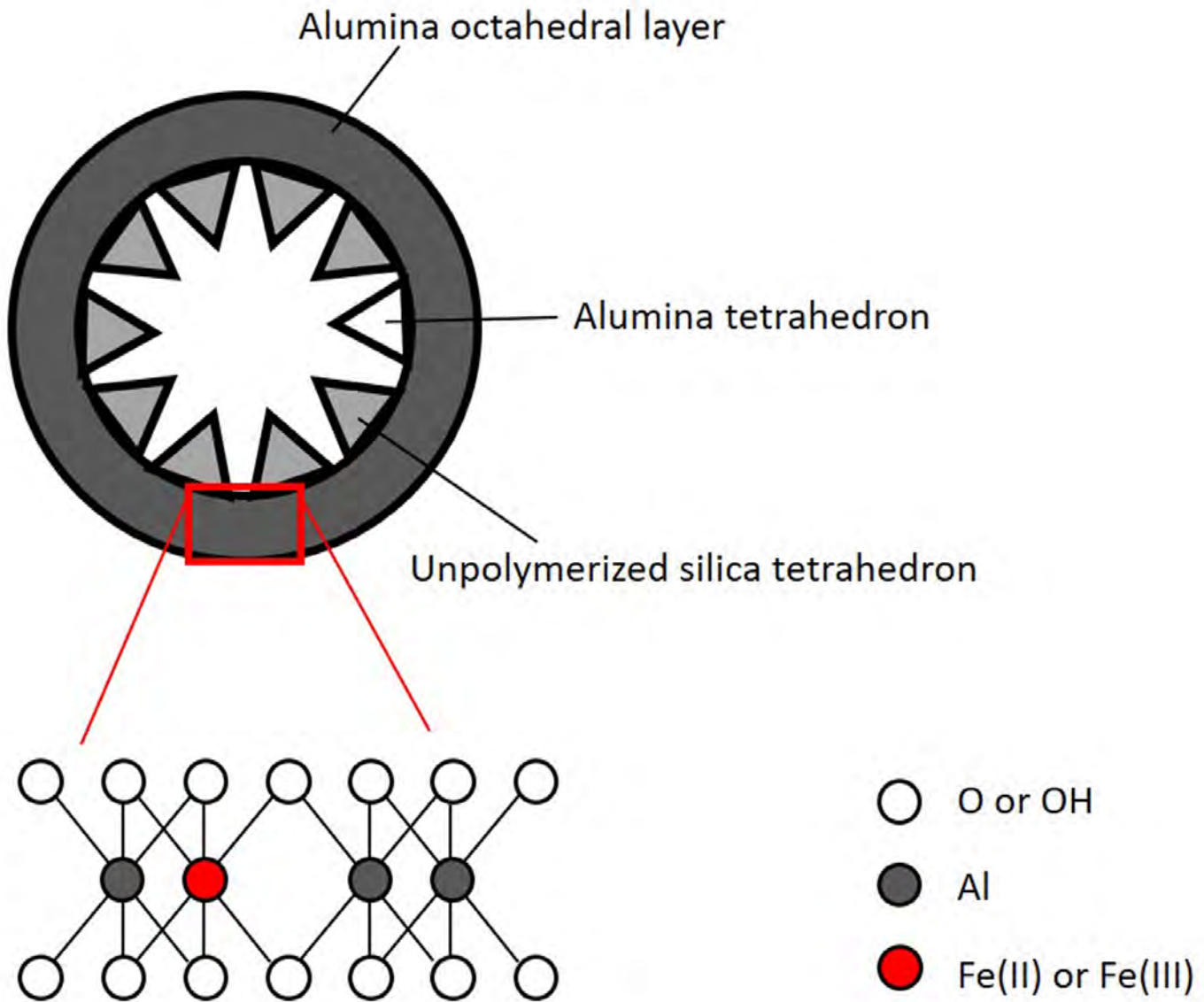


**Fig 2**

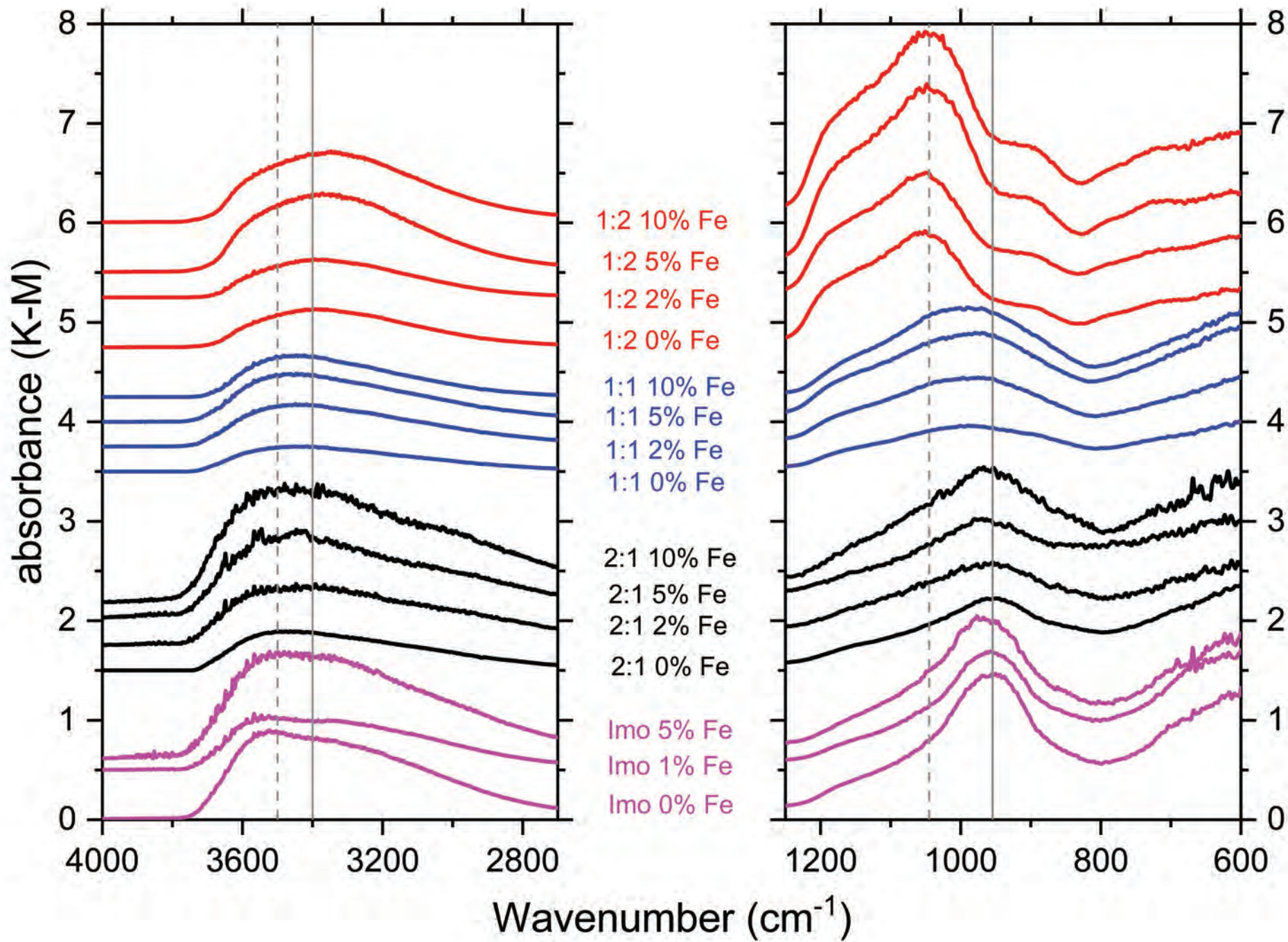




**FIG 3**

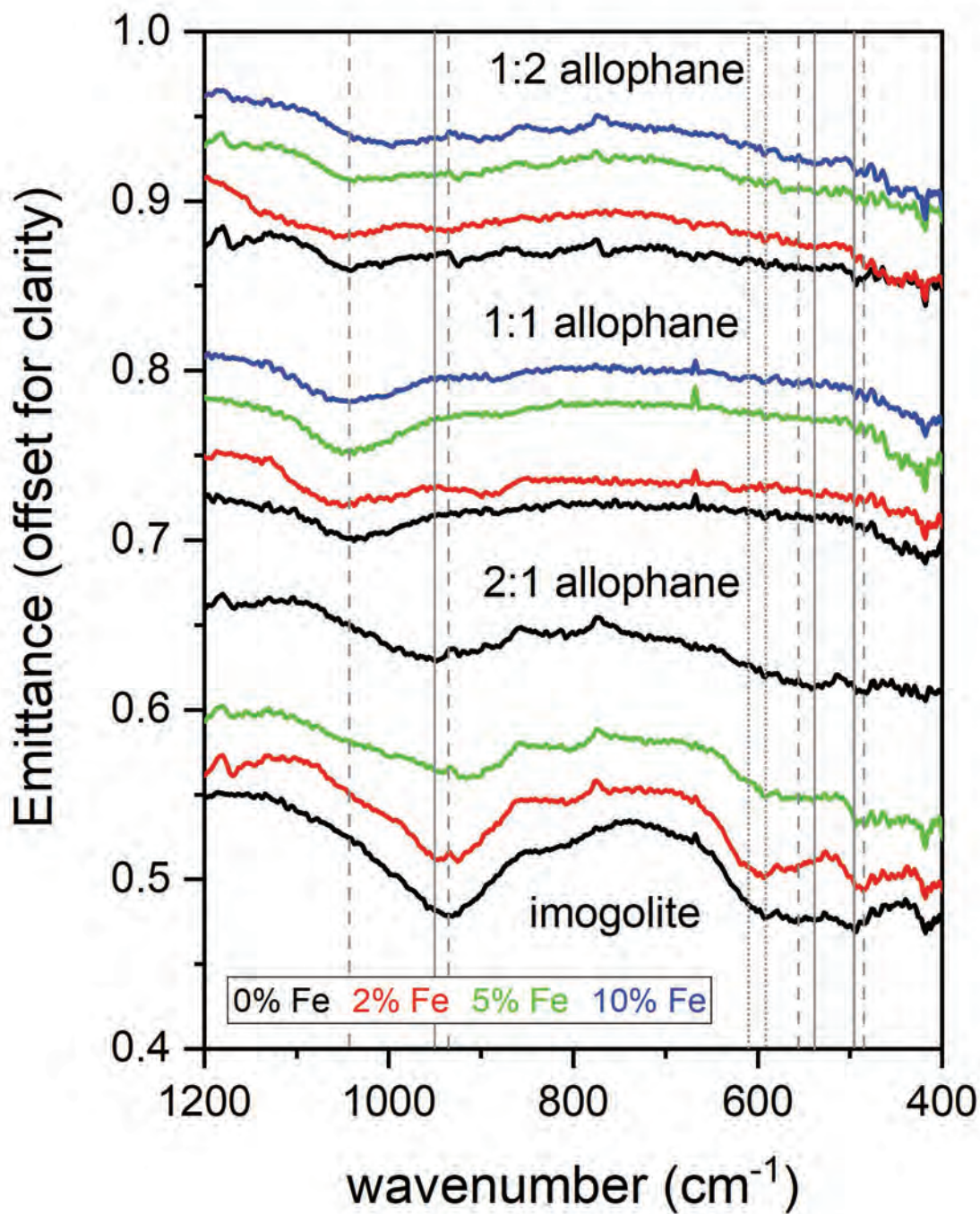


**FIG 4**

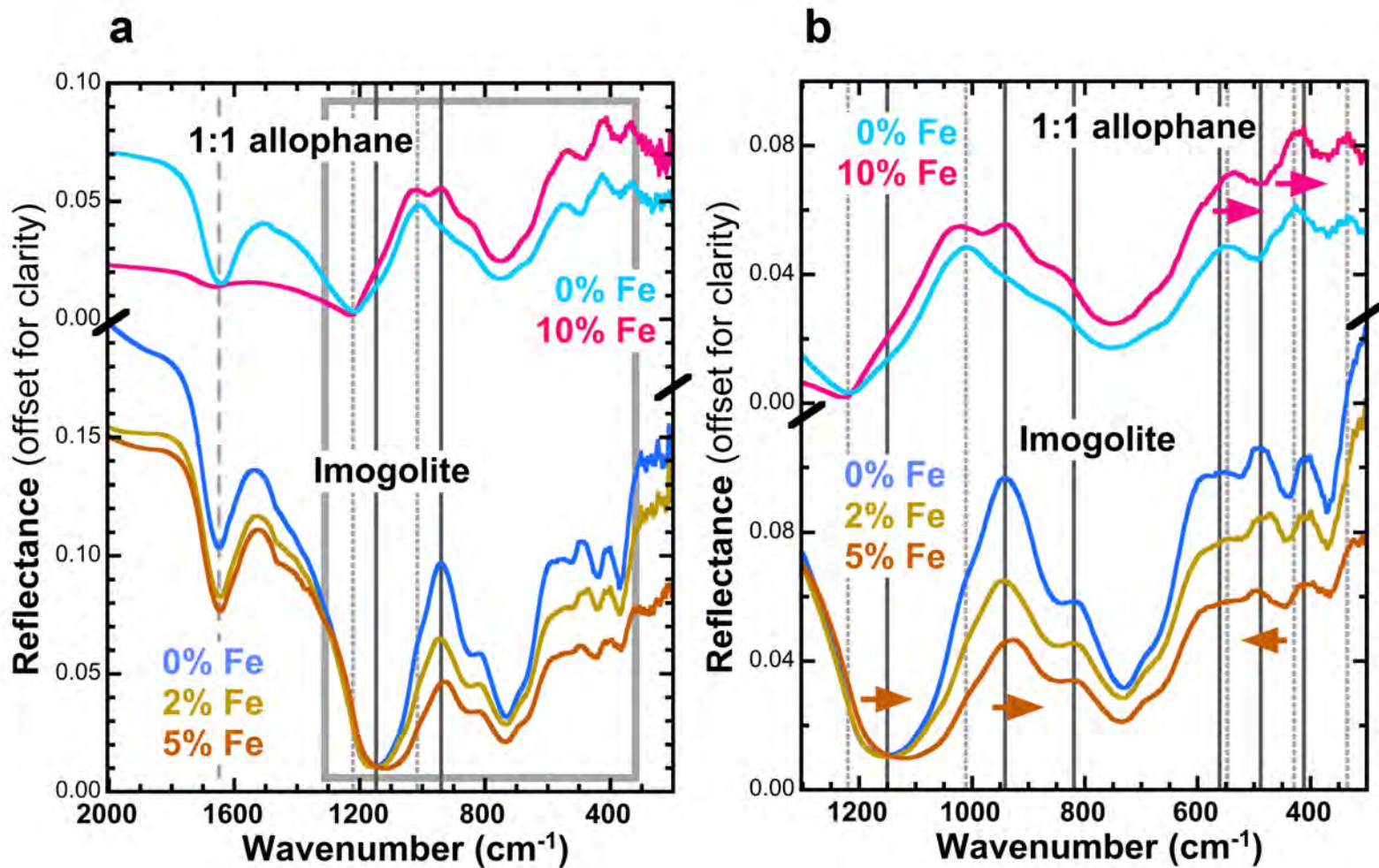




**Fig 5**

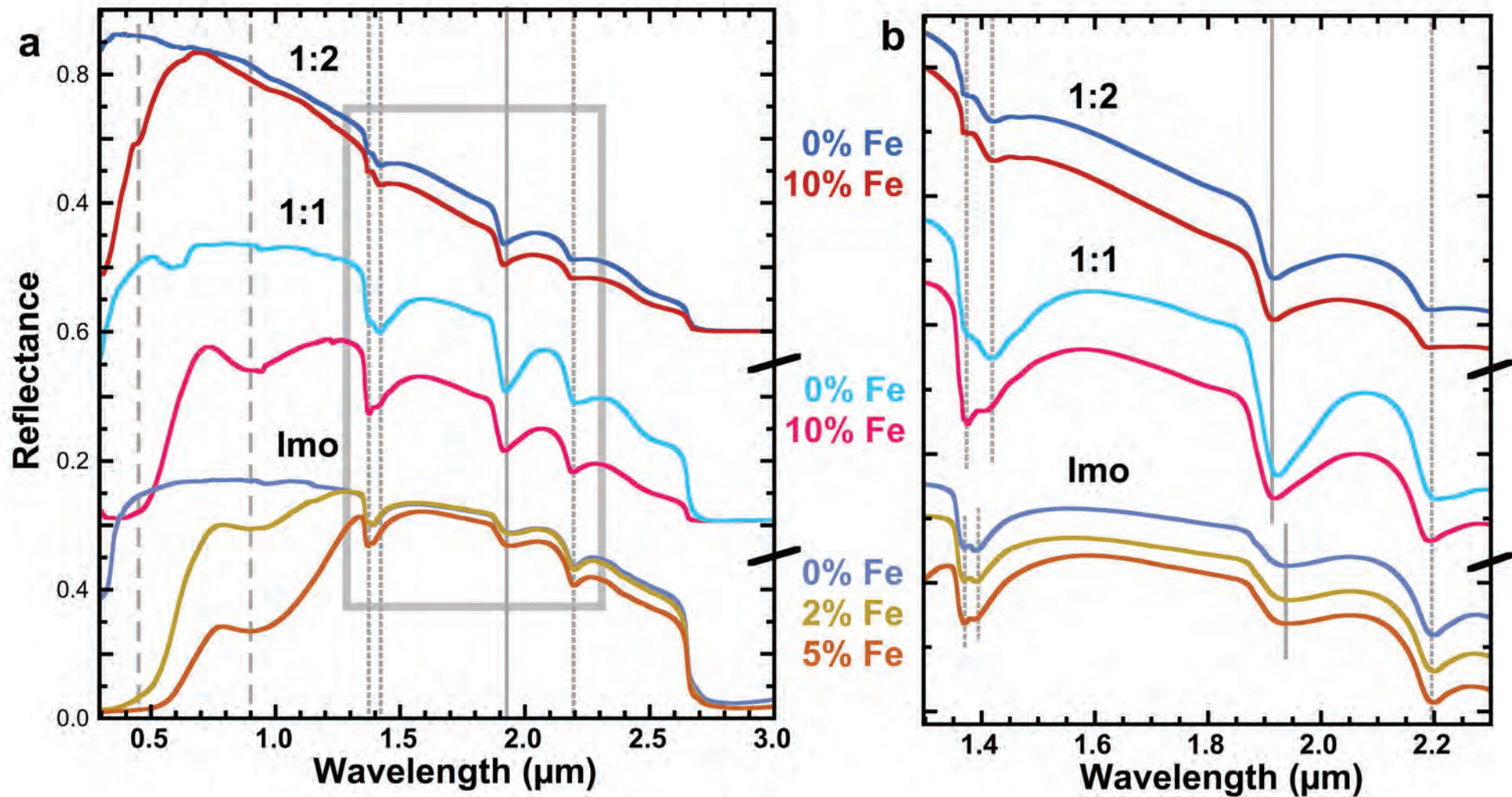


**FIG 6**

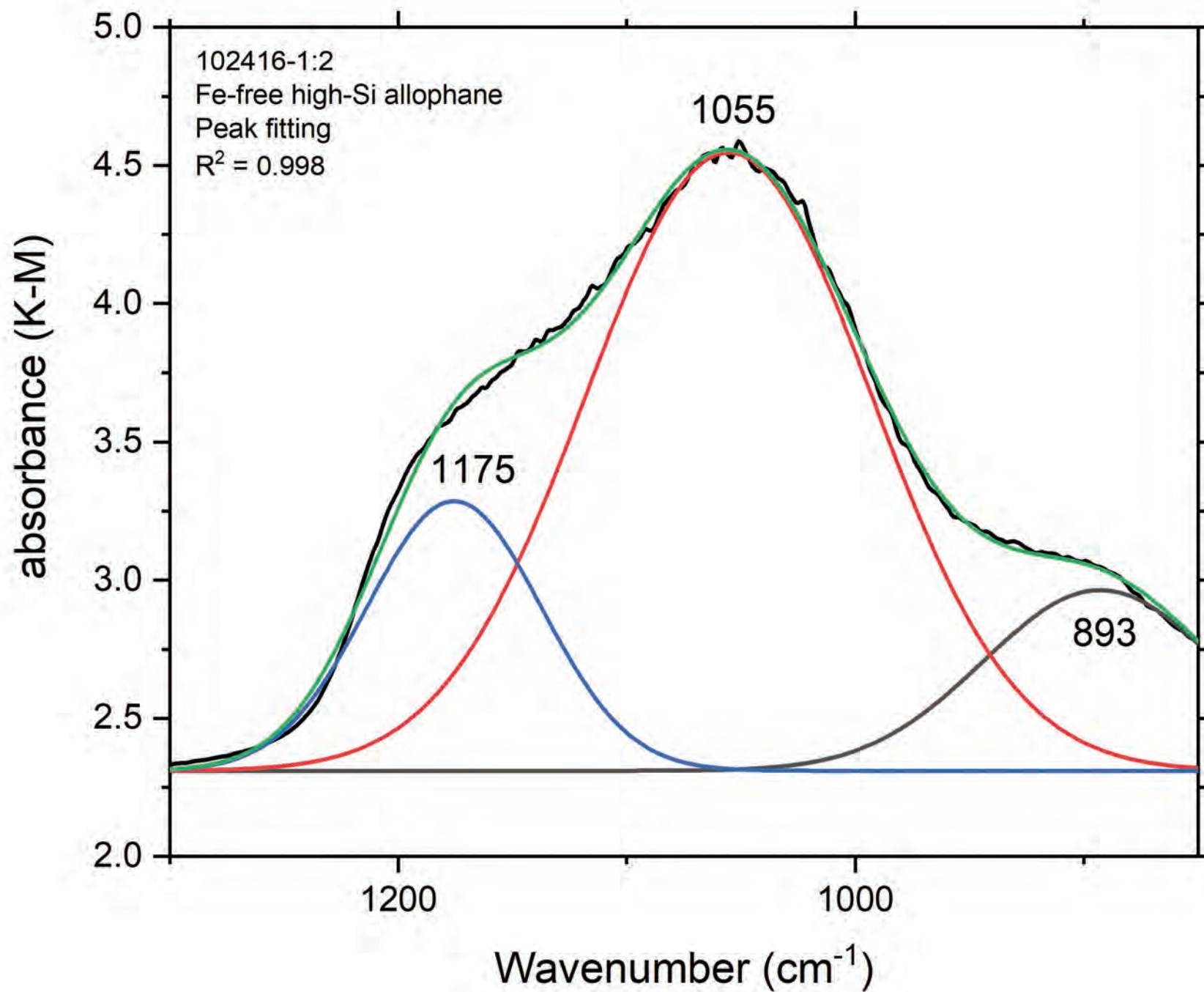


**FIG 7**

$^{27}\text{Al}$  NMR Spectra

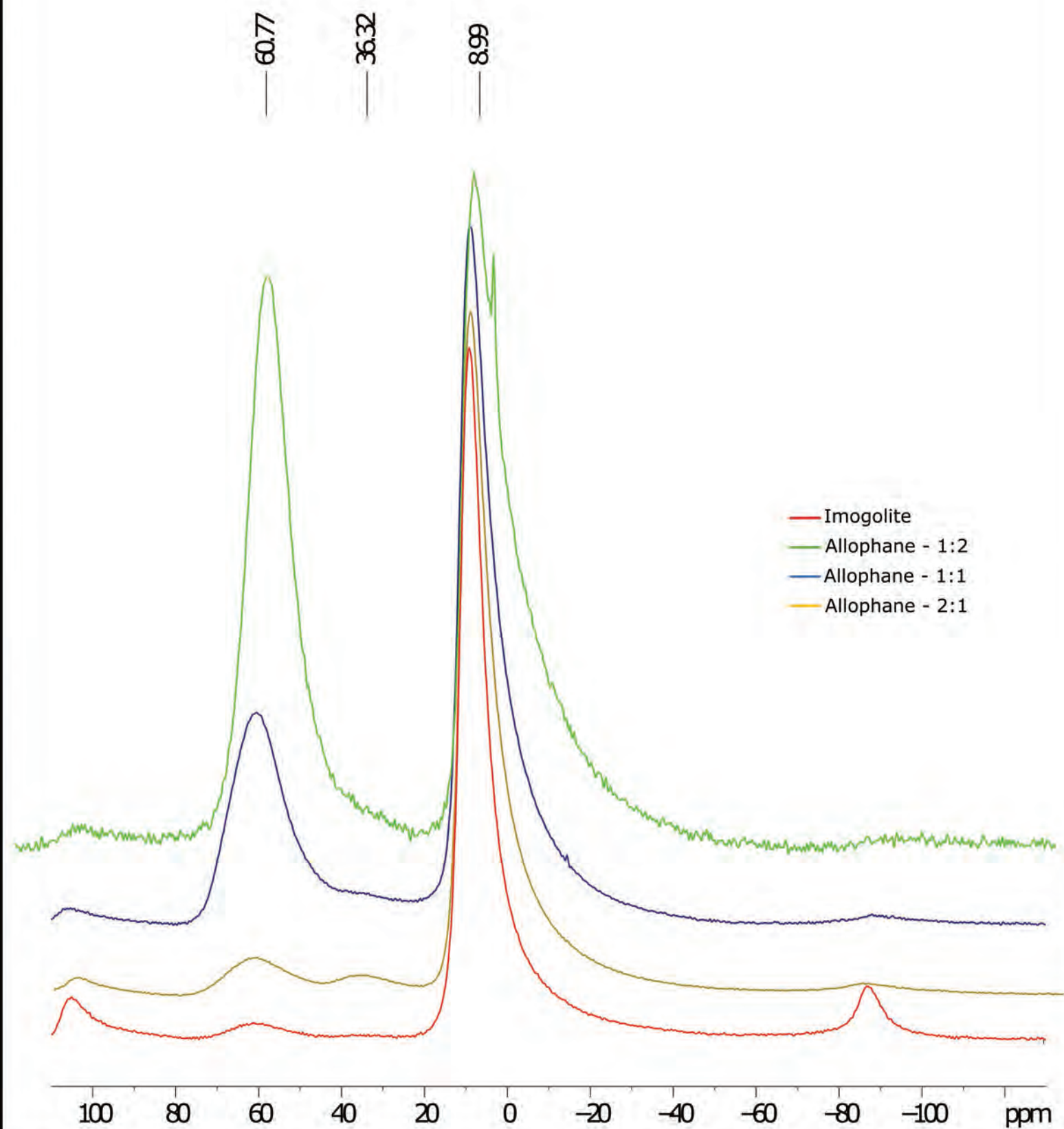




**FIG 8**

$^{29}\text{Si}$  NMR Spectra

— -78.38  
— -86.42  
— -90.01  
— -99.54

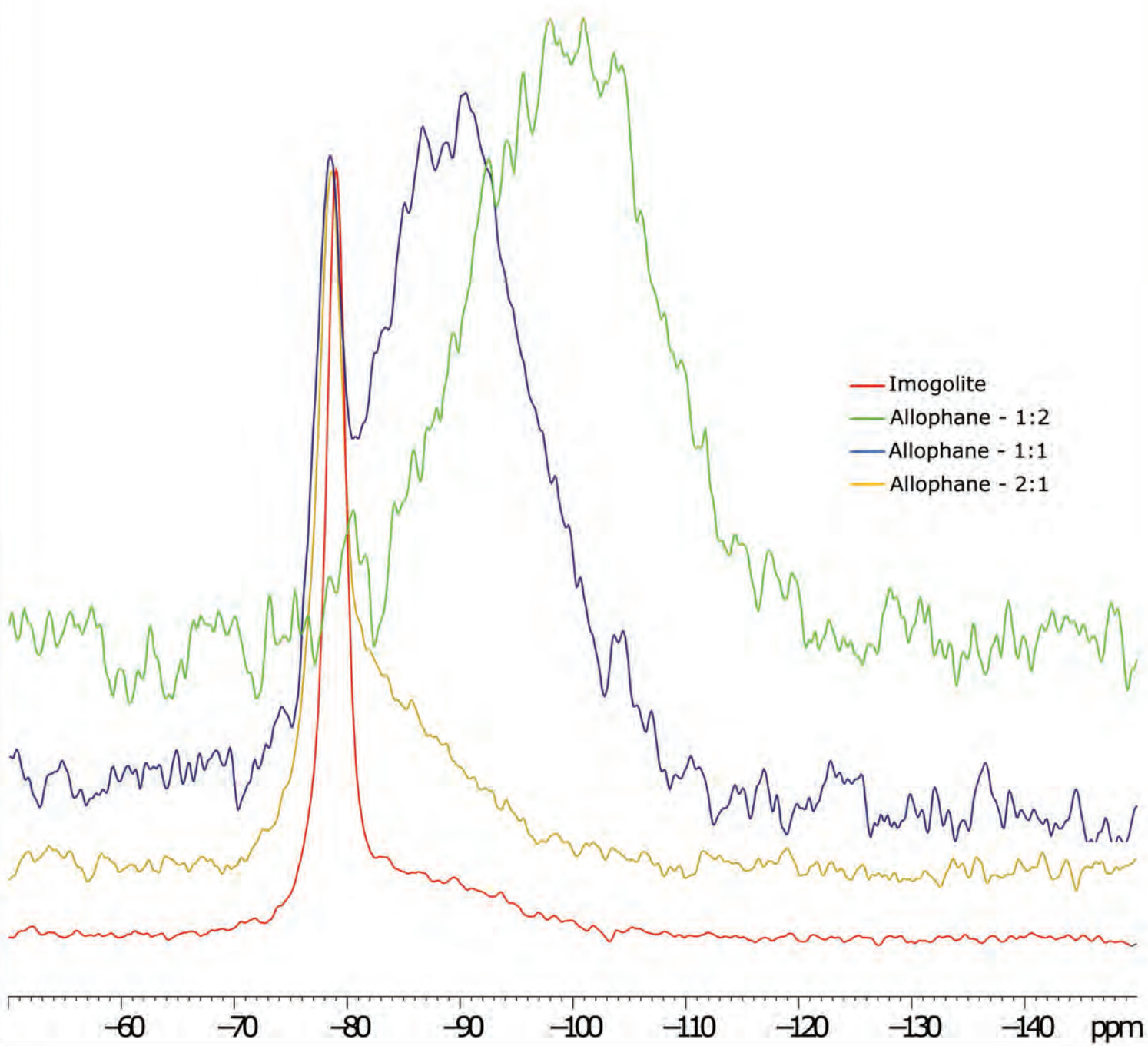




# FIG 9

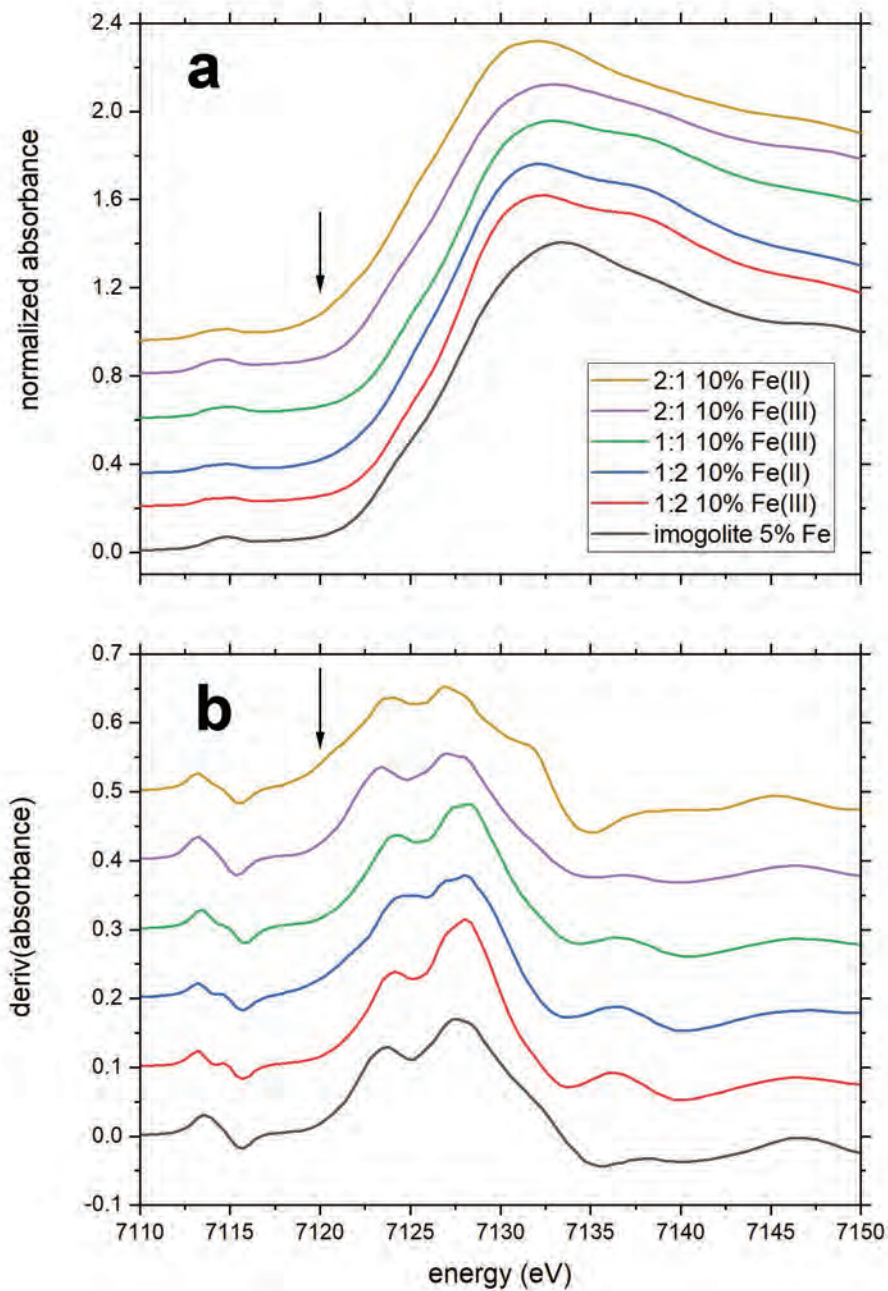


# FIG 10

